MACHINE LEARNING ALGORITHMS FOR BEAM COMPENSATION AND TRACKING IN FREE-SPACE OPTICS SYSTEMS

Felipe Hugo Braga Bittar

Thesis submitted to the Postgraduate Program in Instrumentation and Applied Optics of the Federal Center for Technological Education of Rio de Janeiro, CEFET/RJ, and Federal Fluminense University as partial fulfillment of the requirements for the degree of doctor.

Advisor: Vinicius Nunes Henrique Silva (UFF/Brazil)
coadvisors: Andres Pablo Lopez Barbero (UFF/Brazil)
Fernando Pedro Pereira Guiomar (IT/Portugal)
Paulo Miguel Nepomuceno Pereira Monteiro (IT & UA/Portugal)

Rio de Janeiro,

February 2026

Ficha catalográfica elaborada pela Biblioteca Central do CEFET/RJ

B624 Bittar, Felipe Hugo Braga
Machine learning algorithms for beam compensation and tracking in free-space optics systems / Felipe Hugo Braga Bittar. — 2026.
89f. : il. color. , enc.

Tese (Doutorado) Centro Federal de Educação Tecnológica Celso Suckow da Fonseca, 2026.
Bibliografia : f. 84-89
Orientador: Vinicius Nunes Henrique Silva
Coorientadores: Andres Pablo Lopez Barbero, Fernando Pedro Pereira Guiomar, Paulo Miguel Nepomuceno Pereira Monteiro

1. Comunicações ópticas. 2. Aprendizado do computador. 3. ATP (Programa de computador). 4. Redes neurais (Computação). 5. Turbulência atmosférica. I. Silva, Vinicius Nunes Henrique. (Orient.). II. Barbero, Andres Pablo Lopez. (Coorient.). III. Guiomar, Fernando Pedro Pereira. (Coorient.). IV. Monteiro, Paulo Miguel Nepomuceno Pereira. (Coorient.). V. Título.

CDD 621.3692

Elaborada pela bibliotecária Tania Mello – CRB/7 nº 5507/04

MACHINE LEARNING ALGORITHMS FOR BEAM COMPENSATION AND TRACKING IN FREE-SPACE OPTICS SYSTEMS

Thesis submitted to the Postgraduate Program in Instrumentation and Applied Optics of the Federal Center for Technological Education of Rio de Janeiro, CEFET/RJ, and Federal Fluminense University as partial fulfillment of the requirements for the degree of doctor.

Felipe Hugo Braga Bittar

Examining jury:

President, Professor Ph.D. Vinicius Nunes Henrique Silva (UFF/Brazil)

Professor Ph.D. Andrés Pablo López Barbero (UFF/Brazil)

Professor Ph.D. Paulo Miguel Nepomuceno Pereira Monteiro (IT & UA/Portugal)

Professor Ph.D. Maria do Carmo Raposo de Medeiros (IT & UC/Portugal)

Professor Ph.D. Arismar Cerqueira Sodré Junior (INATEL/Brazil)

Professor Ph.D. Amaro Azevedo Lima (CEFET-RJ/Brazil)

Professor Ph.D. Marcelo Eduardo Viera Segatto (UFES/Brazil)

Niterói, February 2026

DEDICATION

Em primeiro lugar, agradeço aos meus Orientadores e Coorientadores, pela confiança, pela orientação segura e pelo apoio constante ao longo do desenvolvimento desta tese.

Agradeço ao Instituto de Telecomunicações (IT-Aveiro), pelo acolhimento institucional e pelo acesso às instalações e recursos laboratoriais, fundamentais para a realização desta investigação.

Registro agradecimento especial ao Professor Doutor Paulo Miguel Nepomuceno Pereira Monteiro, da Universidade de Aveiro e investigador do IT, e à Professora Doutora Maria do Carmo Raposo de Medeiros, da Universidade de Coimbra e colaboradora do IT, pela parceria acadêmica e pelas relevantes contribuições técnicas e científicas.

Aos colegas do LACOP-UFF e aos pesquisadores do Instituto de Telecomunicações, em especial Fernando Guiomar, Gil Fernandes, Antônio Adade e Márcio Garrido, agradeço pelas discussões técnicas e pela cooperação ao longo desta pesquisa.

Agradeço, ainda, à Coordenação de Aperfeiçoamento de Pessoal de Nível Superior (CAPES), pelo apoio financeiro.

A todos, meu sincero agradecimento.

ACKNOWLEDGMENTS

O presente trabalho foi desenvolvido com o apoio da Coordenação de Aperfeiçoamento de Pessoal de Nível Superior - Brasil (CAPES) - Finance Code 001.

RESUMO

Algoritmos de Aprendizado de Máquina para Compensação e Rastreamento de Feixe em Sistemas Ópticos de Espaço Livre

A comunicação óptica em espaço livre (FSO) tem emergido como uma tecnologia habilitadora fundamental para redes sem fio de próxima geração, devido ao seu potencial para suportar taxas de dados extremamente elevadas, operação isenta de licenciamento e segurança intrínseca. Além disso, enlaces FSO apresentam rápida e simples implementação quando comparados a infraestruturas cabeadas, pois não requerem escavação do solo nem solicitação de direito de passagem em postes ou dutos, constituindo uma alternativa atrativa para implantação ágil de enlaces de alta capacidade. Entretanto, o desempenho e a confiabilidade de enlaces FSO terrestres são fundamentalmente limitados por restrições de linha de visada, erros de apontamento e turbulência atmosférica, que introduzem distorções de frente de onda, deslocamento do feixe, alargamento e desvanecimento do sinal. O objetivo desta tese é investigar e demonstrar experimentalmente técnicas ópticas assistidas por aprendizado de máquina para aumentar a resiliência de sistemas de comunicação FSO na camada física, com ênfase particular nos mecanismos de aquisição, rastreamento e apontamento implementados no lado do receptor.

Para esse fim, a tese propõe e valida um conjunto de três subsistemas experimentais complementares, cada um voltado à mitigação de uma limitação crítica em enlaces FSO. Primeiramente, é desenvolvida uma abordagem de rastreamento de feixe baseada em aprendizado de máquina, utilizando triangulação de potência óptica com fototransistores de baixo custo, substituindo solucionadores analíticos convencionais para ampliar a faixa de rastreamento, reduzindo em até 98,5% o tempo de resposta em comparação com métodos tradicionais e apresentando robustez para razões sinal-ruído de até 10 dB. Em segundo lugar, as distorções de frente de onda induzidas pela turbulência atmosférica são mitigadas por meio de uma rede neural convolucional (CNN) integrada a um modulador espacial de luz (SLM), possibilitando a compensação dinâmica da frente de onda e a restauração de um perfil de feixe quase gaussiano no receptor, com aumento da potência óptica média recebida de aproximadamente 35–40% para 85–90% quando comparado ao cenário ideal sem turbulência. Por fim, é introduzido um esquema de compensação de erros de apontamento baseado em SLM, acionado por uma CNN generativa, para o ajuste fino do direcionamento óptico, proporcionando correção não mecânica de desalinhamentos do feixe e ganhos de compensação de apontamento de até 34 dB.

Todas as abordagens são validadas por meio de experimentos em laboratório que emulam os principais efeitos de propagação em comunicações ópticas em espaço livre. De forma geral, os resultados demonstram que o controle de dispositivos ópticos baseado em aprendizado de máquina é capaz de reduzir a latência de resposta e aprimorar a tomada de decisão de controle, aumentando a robustez do processo de aquisição, rastreamento e apontamento (ATP) e resultando em sistemas FSO mais estáveis, adaptativos e resilientes. Parte do desenvolvimento experimental e da análise científica foi realizada em

colaboração internacional com a Universidade de Aveiro e a Universidade de Coimbra, contribuindo para a validação e consolidação dos resultados obtidos nesta tese.

Palavras-chave: Aprendizado de máquina, ATP, Óptica de espaço livre, SLM, Triangulação de potência óptica, Turbulência atmosférica.

ABSTRACT

Machine Learning Algorithms for Beam Compensation and Tracking in Free-Space Optics Systems

Free-space optics (FSO) communication has emerged as a key enabling technology for next-generation wireless networks due to its potential to support extremely high data rates, license-free operation, and inherent security. In addition, FSO links can be rapidly deployed compared with wired infrastructure, as they do not require ground excavation or right-of-way authorization on poles or ducts, making them attractive for fast installation of high-capacity links. However, the performance and reliability of terrestrial FSO links are fundamentally limited by line-of-sight constraints, pointing errors, and atmospheric turbulence, which introduce wavefront distortions, beam wander, beam spreading, and signal fading. The objective of this thesis is to investigate and experimentally demonstrate machine learning (ML) assisted optical techniques for enhancing the FSO communication systems at the physical layer, with particular emphasis on acquisition, tracking, and pointing (ATP) mechanisms deployed at the receiver side.

The thesis proposes and validates a set of three complementary experimental subsystems, each addressing a critical impairment in FSO links. First, a ML-based beam tracking approach is developed using optical power triangulation with low-cost phototransistors, replacing conventional analytical solvers to improve the tracking range and reduce the response time by up to 98.5% compared with traditional methods, while maintaining robustness for signal-to-noise ratios down to 10 dB. Second, atmospheric-turbulence-induced wavefront distortions are mitigated through a convolutional neural network (CNN) integrated with a spatial light modulator (SLM), enabling dynamic wavefront compensation and restoration of a quasi-Gaussian beam profile at the receiver, increasing the received mean optical power from approximately 35–40% to 85–90% relative to the ideal no-turbulence scenario. Third, a generative CNN-driven SLM-based pointing-error compensation scheme is introduced for fine optical steering, providing non-mechanical correction of beam misalignments and pointing-gain improvements of up to 34 dB.

All approaches are validated through laboratory experiments that emulate key FSO propagation impairments. Overall, the results demonstrate that ML-based control of optical devices reduces response latency and improves control decision-making, thereby enhancing the robustness of the ATP process and enabling more stable, adaptive, and resilient FSO communication systems. Part of the experimental development and analysis was conducted in international collaboration with the University of Aveiro and the University of Coimbra, contributing to the validation and consolidation of the results presented in this thesis.

Keywords: ATP, Atmospheric Turbulence, Free-space optics, Machine Learning, Optical power triangulation, SLM.

LIST OF ACRONYMS

5G	fifth-Generation (Wireless Systems)
6G	Sixth-Generation (Wireless Systems)
ANN	Artificial Neural Network
AoA	Angle of Arrival
AT	Atmospheric Turbulence
ATP	Acquisition, Tracking, and Pointing
BER	Bit Error Rate
BS	Beam Splitter
CCD	Charge-Coupled Device
CMOS	Complementary Metal-Oxide-Semiconductor
CNN	Convolutional Neural Network
CV	Computer Vision
D2NN	Diffractive Deep Neural Network
EQS	Iterative Equation System
FFT	Fast Fourier Transform
FoV	Field of View
FSM	Fast Steering Mirror
FSO	Free-Space Optics
GS	Gerchberg–Saxton
IR	Infrared
LC	Liquid Crystal
LG	Laguerre–Gaussian
LOS	Line of Sight
ML	Machine Learning
MLP	Multilayer Perceptron

NI	Normalized Irradiance
OAM	Orbital Angular Momentum
PDF	Probability Density Function
PE	Pointing Errors
PID	Proportional–Integral–Derivative
PM	Power Meter
QPD	Quadrant Photodetector
RX	Receiver
SGD	Stochastic Gradient Descent
SLM	Spatial Light Modulator
SMF	Single-Mode Fiber
SNR	Signal-to-Noise Ratio
TX	Transmitter
UV	Ultraviolet
VB	Vortex Beam
WDM	Wavelength-Division Multiplexing

LIST OF FIGURES

Figure 1 – Block diagram of a terrestrial FSO System. 21

Figure 2 – Bit rate vs. year for FSO systems of field demonstrations, adapted from [7]. 22

Figure 3 – Data rate versus range of commercially available FSO systems (red stars) compared with notable experimental demonstrations (blue diamonds), reproduced from [12]. 23

Figure 4 – Turbulence cascade theory, where L_0 denotes the outer scale and l_0 the inner scale. Eddies between scale sizes l_0 and L_0 form the inertial range, reproduced from [13]. 25

Figure 5 – Beam wander described by movement of the center optical beam, reproduced from [13]. 27

Figure 6 – Log-normal PDF with $E[l] = 0$ and for a range of variance values. 32

Figure 7 – Gamma probability density function with mode=1 and for a range of variance. 33

Figure 8 – Topology of an artificial neural network [17]. 35

Figure 9 – The kernel starts at the top-left corner of the input data. 37

Figure 10 – The kernel moves across the input according to the defined stride. 37

Figure 11 – The kernel completes the convolution operation after scanning the entire input. 37

Figure 12 – Example of convolution operation with a kernel size of 3×3, no padding, and a stride of 2. 37

Figure 13 – The pooling kernel starts at the top-left region of the feature map. 38

Figure 14 – The kernel slides across the feature map according to the stride, selecting the maximum value within each region. 38

Figure 15 – The pooling operation completes after covering the entire feature map, resulting in a spatially reduced representation. 38

Figure 16 – Example of max-polling operation with a kernel size of 3×3, no padding, and a stride of 2. 38

Figure 17 – Receiver project design and 3D-printed. 50
Figure 18 – Experimental setup element devices. 51
Figure 19 – Incident GB characterization with circular profile. 52
Figure 20 – Average SNR in dB as a function of the radial distance from the GB peak. 52
Figure 21 – Areas covered by the different training datasets and the line test data. 53
Figure 22 – Block diagram of the proposed methodology. 55
Figure 23 – Training loss curves of the multiple ANN configurations, using the MSE loss function, versus the number of epochs for different batch sizes and AR. 56
Figure 24 – Dynamic range and average accuracy improvements in the beam-tracking task achieved by ML models compared to traditional EQS. 59
Figure 25 – Models' analysis based on statistical and prediction error across SNR levels. 59
Figure 26 – Model performance comparison: Euclidean error *versus* response time. 60

Figure 27 – CNN for AT compensation. Convolutional layers are represented by the yellow block with dimensions, $D@N \times N$, where D represents the depth and $N \times N$ the layer grid dimension; max-pooling layers are indicated by red blocks; fully connected layers are indicated by blue blocks. 65
Figure 28 – Evolution of the loss function during CNN training versus epochs. 65
Figure 29 – Commercial SLM Pluto-2 manufactured by Holoeye. 66
Figure 30 – Phase modulation (π rad) *versus* gray-scale level for the 18:6 LUT at 1554 nm. 67
Figure 31 – Resulting phase π radians vs. gray level plot for 18:6 sequence and 1554 nm. 67
Figure 32 – Short caption 68
Figure 33 – Coupled power into SMF under different scenarios. 69

Figure 34 – Gaussian beam wavefront interacting with the SLM: (a) propagation without atmospheric turbulence, (b) propagation under atmospheric turbulence, and (c) turbulence compensation using the proposed correction method. 69
Figure 35 – PDFs of the normalized irradiance: (a) fitted distribution and (b) compensated irradiance. 70
Figure 36 – CNN model for PEC. Convolutional and deconvolutional layers are represented by the yellow and green blocks, respectively, with dimensions, $D@N \times N$, where D represents the depth and $N \times N$ the layer grid dimension; max-polling layers are indicated by red blocks. 74
Figure 37 – Evolution of the loss function during the CNN training stage versus the number of epochs. 74
Figure 38 – CNN PE compensation model test stage. 75
Figure 39 – Representative schema of a typical FSO receiver. 76
Figure 40 – Schematic diagram of the experimental setup. M1: movable flat mirror; SLM: spatial light modulator; CCD: charge-coupled device; BS: beam splitter; SMF: single-mode fiber; PM: power meter. 77
Figure 41 – Schematic diagram of the updated experimental setup. M1: movable flat mirror; M2: fixed flat mirror; SLM: spatial light modulator; BS: beam splitter; QD: quadrant position-sensing detector; SMF: single-mode fiber; PM: power meter. 78
Figure 42 – From left to right: displaced GB (0.5 mm), PEC phase mask, and corresponding resulting effect. 79
Figure 43 – Optical power coupled in SMF with PEC ON and OFF. 79
Figure 44 – Gain versus distance displacement. 80
Figure 45 – Descriptive statistical analysis of gain values of the PEC system across a wide range of radial displacement. 80

LIST OF TABLES

Table 1 – Atmospheric attenuation as a function of visibility for different conditions. 24

Table 2 – Comparative analysis of beam tracking techniques for Experiment 1. 45

Table 3 – Comparative analysis of wavefront compensation for Experiment 2. 45

Table 4 – Comparative analysis of pointing error compensation for Experiment 3. 46

Table 5 – Cardinal position of the PT_i. 52

Table 6 – Comparative error metrics MSE and STD of ML models on test dataset. 58

Table 7 – Parameters used for AT phase masks generation for Experiment 2. 64

Table 8 – Parameters used for AT phase masks generation for experiment 3. 73

CONTENTS

Introduction **14**

1 Introduction **14**

1.1 Motivation 17

1.2 Contributions 17

1.3 Outline 19

2 Theoretical foundations of free-space optical communications **20**

2.1 Overview of FSO as an enabling technology 20

2.2 Meteorological effects within free-space channel 23

2.3 Atmospheric turbulence effects within free-space channel 24

2.3.1 Beam wander, spreading, and scintillation 27

2.4 Channel irradiance modeling 29

2.4.1 Lognormal model 30

2.4.2 Gamma model 33

2.5 Machine learning algorithms 34

2.5.1 Artificial neural networks 34

2.5.2 Convolutional neural networks 36

2.5.3 Linear regression 39

2.5.4 K-nearest neighbors 40

2.6 Literature review of tracking, pointing error and wavefront-compensation methods 41

3 Experiment 1: ML-driven FSO tracking error mitigation **48**

3.1 Theory background and methodology 50

3.1.1 Experimental FSO system characterization 51

3.1.2 Data acquisition and transformation 53

3.1.3 Machine learning models 54

3.2 Results 55
3.2.1 Tuning the number of ANN training epochs 55
3.2.2 Models accuracy 57
3.3 Conclusion 60

4 Experiments 2 and 3: ML–Driven SLM for wavefront turbulence and pointing error compensation 62
4.1 ML–Driven SLM for wavefront turbulence 62
4.1.1 Introduction 62
4.1.2 Theory Background and methodology 63
4.1.3 Results 68
4.1.4 Conclusion 70
4.2 ML–Driven SLM for pointing error compensation 71
4.2.1 Introduction 71
4.2.2 Theory background and methodology 72
4.2.3 Results 78
4.2.4 Conclusion 80

5 Thesis conclusion 82

1- Introduction

As network connectivity becomes increasingly dense, the demand for high-capacity and reliable data transmission has intensified. According to Statista estimates, the global volume of data created, captured, copied, and consumed is expected to increase sharply, from an estimated 173.4 zettabytes in 2025 to 527.5 zettabytes by 2029, more than tripling over four years [1]. This unprecedented growth in data traffic, combined with the rapid densification of radio-frequency (RF) access networks and the inherent limitations of the spectrum, has motivated the adoption of Free-Space Optics (FSO) as a complementary wireless technology.

FSO is a promising enabling technology, as it has the potential to support high data rates, with throughputs on the order of terabits per second (Tbps). In fact, FSO is already an in-use technology, for instance, in space communications, including inter-satellite links and satellite-to-ground optical feeder links [2]. These implementations demonstrate that optical beam propagation over long distances is feasible and reliable when appropriate acquisition, tracking, and pointing (ATP) mechanisms are employed. Consequently, FSO should be interpreted not as a replacement for RF systems, but as a complementary high-capacity layer in heterogeneous wireless architectures.

Next-generation communication for 5G-advanced, sixth-generation (6G), and beyond systems aims to support Tbps-class data rates, ultra-low latency, and integrated sensing and communication. To achieve these requirements, RF systems are progressively moving toward higher carrier frequencies, namely millimeter waves (30–300 GHz) and sub-terahertz bands (100–300 GHz) [3–5]. These bands provide wider bandwidth but suffer from increased propagation losses, molecular absorption, blockage sensitivity, and strict beam alignment requirements.

In this context, FSO occupies a distinct and synergistic position. While mmWave and sub-THz links extend traditional RF paradigms into higher frequencies, FSO operates in optical frequencies (in the order of hundreds of THz), enabling orders-of-magnitude larger available bandwidth and extremely narrow beam divergence. In addition, RF technology is positioned in the access layer network, while FSO naturally addresses the

transport layer, such as core and backhaul links, where fiber deployment is impractical, and RF spectrum is congested. Thus, in terrestrial networks, RF links provide robustness under adverse weather, while FSO provides peak throughput under clear conditions. Hybrid RF/FSO systems dynamically switch or aggregate channels depending on atmospheric conditions, significantly improving link availability.

Notably, the FSO market is already established, and numbers released by Fortune Business report a FSO market size of approximately $ 313.8 million and a projected Compound Annual Growth Rate (CAGR) of 16.6% from 2025 to 2032 [6]. Despite this potential, the reliability of FSO systems remains fundamentally constrained by the characteristics of the free-space propagation medium.

In fact, in terrestrial FSO communication systems, the optical beam propagation is significantly affected by atmospheric turbulence (AT). AT is an inherent phenomenon in FSO links and arises from random fluctuations in the refractive index of air caused by spatial and temporal variations in local temperature and pressure [7]. These fluctuations, commonly modeled by Kolmogorov cascade theory, give rise to air eddies of different scales that interact with the propagating optical wavefront. As a result, several deleterious effects are observed, including beam wander, beam spreading, scintillation, and consequently wavefront distortions, all of which degrade link performance and system reliability.

In this context, this thesis focuses on enhancing the resilience of FSO communication systems by addressing AT-induced physical-layer impairments. The proposed approaches are developed and validated through experimental setups, in which ML-based control strategies are employed to operate optical devices and mitigate AT-induced distortions. The effectiveness of these strategies is assessed through their impact on physical-layer performance metrics, thereby providing practical insights into the design of more robust FSO communication links.

This thesis presents three experimental investigations focused on improving ATP strategies for FSO communication systems. The ATP framework encompasses a set of systems and subsystems designed to enhance the reliability and robustness of the line-of-sight (LOS) requirement inherent to FSO technology. All experiments were conducted to improve the quality of the received optical signal power and, consequently, the overall physical-layer performance. To this end, the proposed strategies are implemented at the receiver (RX) side, thereby providing forward compensation for impairments introduced by the AT channel. It is essential to note that the experiments are not independent, but rather

form a concatenated processing chain of functionally interdependent subsystems. This interdependence within the overall system architecture is discussed in detail in subsequent sections of the thesis.

The first experiment (experiment 1) proposes a movable rectangular plane at the RX-side for optical beam tracking based on an optical power triangulation method using low-cost phototransistors. This method traditionally employs iterative numerical solvers to solve a set of nonlinear equations. Therefore, replacing the traditional computational solver method with machine learning (ML) models, such as artificial neural networks, linear regression, and k-nearest neighbors, can achieve faster convergence, enhanced noise robustness, and an extended tracking range. By reducing processing latency and hardware complexity, this work supports the development of cost-effective and scalable FSO receiver architectures, particularly when combined with turbulence mitigation strategies at the physical layer. However, the effectiveness of the optical power triangulation method relies on the assumption that the received optical beam exhibits a circular quasi-Gaussian spatial profile at the RX side. In practical FSO scenarios, this condition is violated due to wavefront distortions induced by AT. As a result, reliable beam tracking based on optical power triangulation requires a preceding wavefront compensation stage; therefore, experiment 2 is capable of restoring the beam profile before the execution of the tracking system.

Experiment 2 addresses the issue of compensating the wavefront distorted by AT-induced impairments through the combined use of a convolutional neural network (CNN) for generating phase masks for AT compensation applied to a Spatial Light Modulator (SLM) screen. The key contribution of this work is the experimental demonstrates that deep learning techniques can replace classical iterative wavefront-correction algorithms, such as stochastic gradient descent (SGD) and the Gerchberg–Saxton (GS) algorithms, while significantly reducing computational complexity enabling near–real–time operation, by replacing the conventional iterative numerical solvers and time consuming algorithms by feedforward functions, such as CNN structures. Furthermore, the study provides a detailed statistical analysis of the received irradiance model, showing that after compensation, the Generalized Extreme Value (GEV) distribution more accurately characterizes the channel behavior than traditional turbulence models. This finding contributes to improved modeling and understanding of compensated FSO channels under atmospheric turbulence. Therefore, after wavefront compensation, the optical-power-triangulation tracking stage

can operate under conditions suitable for subsequent pointing error compensation (PEC), which will be addressed in experiment 3.

Experiment 3 introduces an innovative approach for pointing error compensation (PEC) in FSO communication systems by integrating an SLM with a generative CNN. The main contribution of this work lies in replacing conventional analytical grating-based beam deflection manipulation with a CNN capable of learning the nonlinear relationship between radial beam misalignments and the corresponding phase masks required for optical PEC. Experimental results demonstrated substantial improvements in single-mode fiber (SMF) coupling efficiency, achieving compensation gains of up to 34 dB for beam displacements exceeding 4 mm. These results highlight the effectiveness of ML-based optical control for enhancing physical-layer robustness in FSO links subject to dynamic misalignment, and together, the three experiments constitute an integrated ATP for enhancing the resilience of FSO communication systems.

1.1- Motivation

The motivation for this thesis is to study the atmospheric channel, identify research gaps, and investigate techniques to mitigate AT effects on optical beams propagating in free-space channels by exploiting electro-optical devices controlled by ML algorithms. This work focuses on understanding how such device-control strategies can enhance physical-layer robustness and clarify related limitations.

1.2- Contributions

The contributions are applicable to a broad range of FSO architectures and deployment scenarios, including terrestrial transport and backhaul networks. They also extend to non-terrestrial and hybrid systems (e.g., ground-to-satellite links and high-altitude platforms) and to underwater optical wireless communication systems. Thus, through experimental ML-based validation, this work provides practical insights that advance AT

mitigation strategies while contributing to knowledge dissemination within the academic community. In summary, the following list presents the main accomplishments and scientific contributions of this Ph.D., which are enumerated according to the experiment number.

1. Bittar, F. B.; Garrido, M.; Barbero, A. P. L.; Ferreira, T. N.; Silva, V. N. H. Machine learning algorithms for triangulation-based optical beam tracking in FSO systems. *Optics and Lasers in Engineering*, vol. 196, Art. no. 109397, 2026.

2. Bittar, F. B.; Fernandes, G. M.; Barbero, A. L.; Monteiro, P. P.; Guiomar, F. P.; Silva, V. N. H. AI-driven atmospheric turbulence compensation and channel modeling in FSO systems. *Proceedings of the 2025 SBFoton International Optics and Photonics Conference (SBFoton IOPC)*, São Pedro, Brazil, pp. 1-3, 2025.

3. Bittar, F. B., Correia, V. F., Fernandes, G. M., Barbero, A. L., Monteiro, P. P., Guiomar, F. P., Henrique Silva, V. N. Mitigation of Pointing Errors in FSO Systems Through AI-Driven Spatial Light Modulation. *IEEE Photonics Technology Letters*, vol. 37, Art. no. 16, pp. 925-928, 2025.

Regarding [8], this thesis extends optical-power triangulation techniques by integrating ML models for beam tracking and replacing iterative numerical solvers, enabling robust operation under noisy measurements, extending the tracking dynamic range, reducing response time, and providing a low-cost alternative to quadrant photodetectors. Regarding [9], it investigates ML-based atmospheric turbulence wavefront compensation and channel modeling, showing an increase in the received mean optical power from approximately 35–40% to 85–90% relative compared to the ideal no-AT scenario. Paper [10] demonstrates an AI-driven spatial light modulation approach for PE compensation, achieving optical power gains of up to 34 dB for a 0.5 mm beam misalignment and significant performance improvements for displacements up to 4.8 mm. Therefore, this thesis presents three experiments, all of which share the application of ML-driven techniques for the automation of FSO systems, resulting in reduced processing time and increased received optical power

1.3- Outline

Chapter 1 introduces the research context, motivation, objectives, and principal contributions. Chapter 2 establishes the theoretical foundations of FSO communications, AT effects, channel modeling, and ML algorithms employed in the experimental studies. Chapters 3–4 present the three core experimental investigations, each addressing a distinct aspect of ATP resilience in FSO systems: Chapter 3 develops ML models for RX-side beam tracking via optical power triangulation, replacing iterative numerical solvers to enhance dynamic range, response time, and noise robustness; Chapter 4 demonstrates CNN-driven SLM compensation of AT-induced wavefront distortions, with statistical analysis of post-compensation irradiance, and introduces a CNN combined with SLM for phase masks generation implementation for non-mechanical PEC. Finally, the concluding chapter synthesizes the findings, discusses their implications for resilient FSO architectures, and outlines future research directions.

2- Theoretical foundations of free-space optical communications

This chapter is organized as follows: Section 2.1 provides a brief overview of FSO communication as an enabling technology for modern telecommunications and outlines its principal application scenarios. Section 2.2 discusses the main meteorological and atmospheric channel impairments that affect the performance and reliability of FSO systems. Section 2.3 presents the core theoretical background of this thesis, examining the physical origins of atmospheric turbulence and refractive index fluctuations, which are primary sources of performance degradation in optical propagation. Section 2.4 explores irradiance channel modeling. Section 2.5 describes the machine learning algorithms employed throughout the experimental investigations of this thesis. Finally, Section 2.6 provides an overview of the literature review and the comparative techniques utilized in this thesis. Together, these sections establish the theoretical framework required to understand the propagation challenges addressed in the subsequent chapters and to support the design and interpretation of the experimental results presented in this work.

2.1- Overview of FSO as an enabling technology

FSO links are point-to-point connections that employ coherent laser beams, typically in the infrared spectrum, e.g., wavelengths spanning from 1310 up to 1550 nm, with transmission ranges on the order of a few kilometers. Figure 1 illustrates a simplified FSO link comprising transmitter (TX), an atmospheric channel, and a RX. It is worth noting the impairments associated with FSO communication links, such as beam wander, spread, absorption, scintillation, wavefront corruption, and induced PE due to mechanical fatigue material, which can be seen as a sum of input errors and optical power loss to the system.

The TX converts the electrical signal into an optical signal and modulates the

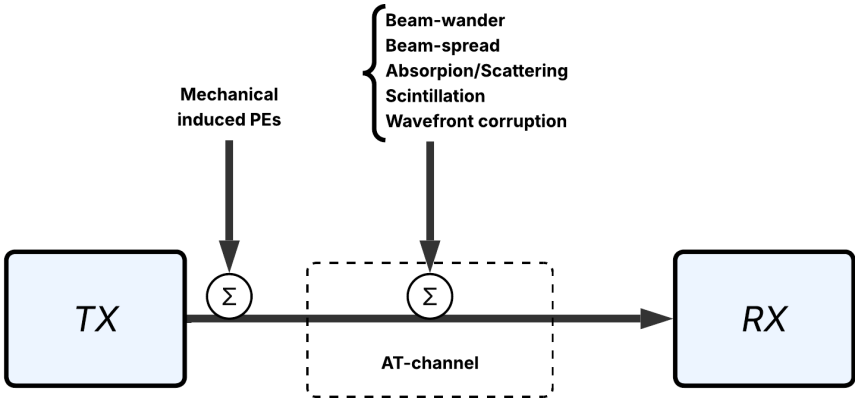


Figure 1 – Block diagram of a terrestrial FSO System.

laser beam to convey data to the receiver through the atmospheric channel. TX typically consists of an optical source, a laser driver circuit, a modulator, and a transmit collimating lens. The optical carrier is provided by a coherent laser diode emitting a narrow linewidth at a millimeter diameter optical signal, commonly implemented using solid-state or semiconductor technologies such as Fabry–Pérot or distributed-feedback lasers.

The propagation medium is the atmosphere, which consists of gaseous layers surrounding the Earth. Within the troposphere, which is the typical layer for terrestrial FSO communications, the atmospheric composition is dominated by nitrogen (N_2, approximately 78%), oxygen (O_2, approximately 21%), and argon (Ar, approximately 1%). In addition, trace constituents such as water vapor (H_2O, ranging from 0 to 7%) and carbon dioxide (CO_2, approximately 0.01 to 0.1%) are present. The atmosphere also contains suspended particulates, commonly referred to as aerosols, including haze, fog, dust, and soil particles [11].

The receiver front-end aperture is typically composed of a convergent optical element, such as a lens or telescope, which captures the incident optical beam after propagation through the AT channel. A receiver aperture that is large relative to the beam width is generally desirable, as it enables the collection of multiple uncorrelated optical wavefronts and directs their averaged irradiance onto the photodetector. This aperture averaging effect improves the received signal quality and enhances robustness against turbulence-induced irradiance fluctuations. Notably, the full data rate potential of FSO systems is realized when signal processing is performed entirely in the optical domain, thereby avoiding delay bottlenecks associated with optical-to-electrical conversion [7].

FSO has attracted increasing interest from both academia and industry as a key enabling technology for diverse applications and is widely regarded as a promising

candidate for 5G-advanced, 6G, and beyond technologies, offering terabit-per-second data rates, as shown in Fig. 2.

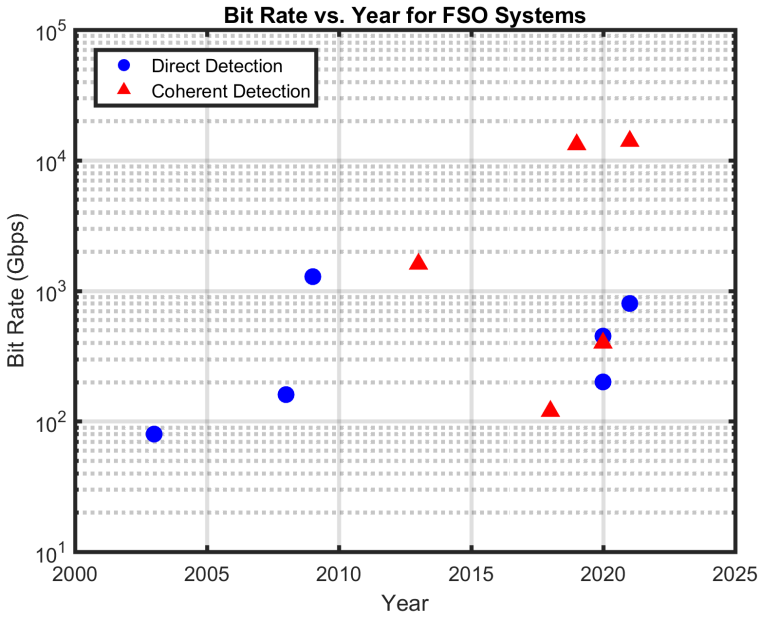


Figure 2 – Bit rate vs. year for FSO systems of field demonstrations, adapted from [7].

Indeed, numerous experimental demonstrations of FSO systems have been reported in the literature. For illustrative purposes, Fig. 3 presents a comparative assessment of the performance potential of FSO as a key enabling technology for access, transport, and backhaul networks. Specifically, the Figure 3 contrasts the data rate versus transmission range achieved by commercially available FSO systems with representative experimental demonstrations.

Regarding FSO applications, one of the most promising approaches is the hybrid use of RF and FSO technologies. The increasing demand for higher data rates in wireless communication systems is pushing standalone RF technologies toward their fundamental physical limits, thereby driving the need for alternative high-capacity solutions. In this context, FSO has emerged as a strong complement to RF communication, enabling hybrid RF/optical wireless networks capable of delivering unprecedented data rates [7]. This integration enhances network capillarity and promotes architectural flexibility.

In addition, the combination of coherent optical communication techniques with advanced modulation formats and digital signal processing has recently emerged as a highly promising approach, particularly when associated with multichannel transmission schemes such as wavelength-division multiplexing (WDM) or by exploiting spatial

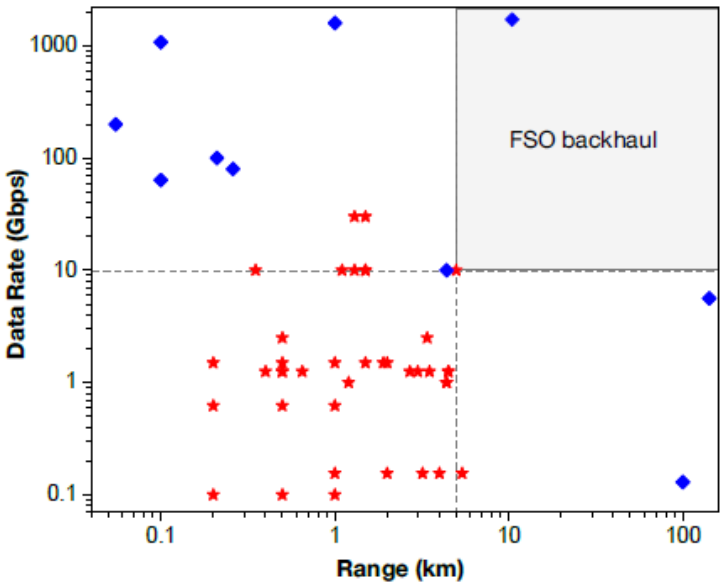


Figure 3 – Data rate versus range of commercially available FSO systems (red stars) compared with notable experimental demonstrations (blue diamonds), reproduced from [12].

diversity [12]. However, fully realizing the potential of FSO transmission requires seamless integration between wireless optical links and fiber-based communication systems. Achieving this objective critically depends on understanding and addressing the dominant limitations imposed by the atmospheric propagation channel.

2.2- Meteorological effects within free-space channel

Despite its advantages, FSO technology faces inherent challenges associated with free-space propagation. Meteorological phenomena such as rain, fog, snow, and haze induce absorption and scattering of the transmitted optical signal, leading to significant attenuation. These effects arise from interactions between the propagating optical beam and atmospheric molecules and aerosols suspended along the transmission path, and, under severe conditions, may even result in a complete link outage. Consequently, FSO communication links are highly sensitive to environmental conditions.

Table 1 summarizes typical atmospheric attenuation values caused by absorption and scattering due to water droplets and aerosols for different visibility conditions [12]. It is worth noting that in clear-air conditions, the lowest attenuation is yielded and therefore

enables the longest FSO link ranges, whereas fog introduces severe attenuation that limits link availability independently of wavelength. These results confirm that meteorological absorption is a primary constraint for terrestrial FSO deployment. However, even when attenuation is negligible, link performance remains limited by AT, which distorts the optical wavefront and degrades alignment stability. Consequently, this thesis focuses on turbulence-induced impairments rather than weather absorption, since AT persists under clear-sky conditions and becomes the dominant limiting factor in high-availability FSO systems

Atmospheric Condition	Visibility [km]	Attenuation [dB/km] at 850 nm	Attenuation [dB/km] at 1550 nm
Clear air	23	0.42	0.2
Haze	4	2.8	1.6
Mist	2	6	4
Light fog	1	13	9
Moderate fog	0.5	28	21
Dense fog	0.2	73	60
Heavy fog	0.05	309	272

Table 1 – Atmospheric attenuation as a function of visibility for different conditions.

2.3- Atmospheric turbulence effects within free-space channel

In addition, AT phenomena are characterized by random fluctuations in the refractive index, and they significantly increase the occurrence of fading and pointing errors. These adverse phenomena impose stringent challenges in achieving and maintaining precise optical beam alignment. The AT is an inherent characteristic of outdoor FSO links. Its main effects include beam wander, spread and scintillation. Variations in atmospheric temperature and pressure create inhomogeneities in the refractive index along the propagation path, which distort the phase front of optical beams. Physically, the atmosphere can be modeled as a dynamic medium composed of eddies that randomly deflect the optical wavefront. The strength of turbulence is commonly quantified by the refractive index structure parameter (C_n^2), which directly impacts key communication metrics such as the bit error rate (BER) and signal-to-noise ratio (SNR) [13].

The AT phenomena modeling treats the atmosphere air as a viscous fluid. The turbulence is fundamentally nonlinear and governed by the Navier-Stokes equations. Thus due to the difficulty of solving such equations, Kolmogorov, in 1940, suggested a subclass

of air vortexes leading to a statistical and mathematical consistency that can receive a simplified theoretical treatment [13].

The vortices proposed by Kolmogorov are generated close to heated surfaces. Then, due to the temperature difference between the ground and the surrounding air and the influence of inertial forces, the vortices move away from the ground. In the sequence, the larger vortexes are broken into smaller vortexes as they move up, and the smaller vortexes start to move independently of their original, causing a redistribution of the kinetic energy of the air and the refractive index of the path link medium crossed by the light beam. The region where the largest vortices are found is called the external scale (L_0), and the region that presents the smallest vortices is the internal scale (l_0). Thus, the family of vortexes of smaller sizes than L_0 and greater than l_0 form the inertial subinterval [13]. The energy cascade theory, which explains the structured atmosphere formed by vortices, is represented in Fig. 4,

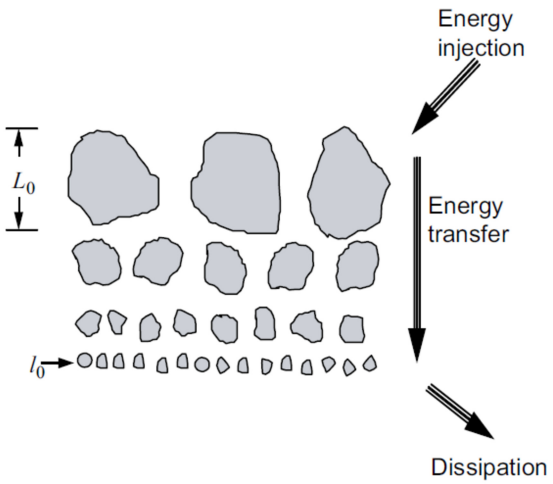


Figure 4 – Turbulence cascade theory, where L_0 denotes the outer scale and l_0 the inner scale. Eddies between scale sizes l_0 and L_0 form the inertial range, reproduced from [13].

The energy cascade theory states that the atmospheric intervals between L_0 and l_0 are statistically homogeneous and isotropic. Therefore, the turbulence vortexes are modeled as random spatial fluctuations of the refractive index correlated with the temperature difference [13]. The index of refraction n is an important parameter of the atmospheric channel for optical wave propagation, and it is sensitive to small-scale temperature fluctuations [13]. Thus, in a particular point in the space R and time t, the index of refraction can be mathematically expressed by Eq. [1], where the mean value of the index of refraction ($n(R,t)$) experiments a random deviation by the random variable n_1,

thus, causing fluctuations in $n(R,t)$ values,

$$n(R,t) = 1 + n_1(R,t). \tag{1}$$

Furthermore, the index of refraction for the atmosphere can be written for optical and IR wavelengths according to Eq. [2] while the time is commonly suppressed in the treatment of optical wave propagation [13].

$$n(R) = 1 + 1 + 77.6 \times 10^{-6}(1 + 7.52 \times 10^{-3}\lambda^{-2})\frac{P(R)}{T(R)}, \tag{2}$$

where λ is the optical wavelength in μm, P is the pressure in millibars, and T is the temperature in Kelvin.

The Eq. [2] demonstrates that the wavelength dependence is small for optical frequencies and considering that horizontal links are of interest in this work, the pressure at points of the same height or with small variations are generally neglected, thus making the refractive index sensitive mainly to temperature. Thus, in order to characterize the average refractive index of air channel caused by AT, it is introduced the C_n^2 parameter. Physically, the C_n^2 is a measure of the strength of the fluctuations in the refractive index [13]. The C_n^2 at a point in space along the propagation path can be calculated from the temperature structure function C_T^2 obtained from two temperature measurement points as follow Eq. [3],

$$C_n^2 = \left(79 \times 10^{-6}\frac{P}{T^2}\right)^2 C_T^2. \tag{3}$$

Where the temperature structure function (C_T^2) is obtained using the Eq. [4],

$$< (T_2 - T_1) >= C_T^2 Z^{2/3}. \tag{4}$$

where $<>$ is the ensemble average, T_2 and T_1 denote the temperature at two points separated by distance Z and C_T^2 is the temperature structure constant (in units of $deg^2/m^{2/3}$).

In summary, AT plays a decisive role in the degradation of optical wave propagation, with the C_n^2 parameter serving as a fundamental metric for its characterization. The fluctuations in refractive index directly influence the coherence and stability of the propagating beam, leading to observable manifestations such as beam wander, beam spreading, and scintillation. Therefore, the AT effects are intrinsically linked to both the statistical properties of the medium and the measurable distortions imposed on the optical signal.

This understanding provides the theoretical basis for developing mitigation techniques and system designs that enhance the performance of optical communication under turbulent conditions.

2.3.1 Beam wander, spreading, and scintillation

As a consequence of AT, beam wandering introduces dynamic PEs, which may be further exacerbated by building sway, wind loads, and mechanical instabilities. These impairments degrade the SNR and reduce the achievable data. Additionally, turbulence-induced distortions affecting the intensity, phase, and spatial distribution of the optical beam result in random irradiance fluctuations at the receiver. Thus, understanding these phenomena is essential for optical wireless channel modeling and for the development of effective mitigation strategies aimed at enhancing the reliability and efficiency of FSO communication links.

Beam wander refers to random beam deflections during propagation, causing the spreading of the beam by channel inhomogeneities. Over short periods, the beam profile at the receiver randomly moves off the boresight, and its power distribution is skewed from the Transverse Electromagnetic fundamental mode (TEM_{00}), modeled by a Gaussian, as can be seen in Fig. 5. Then, the instantaneous center of the beam (point of maximum power incidence) is therefore randomly displaced in the receiver plane, producing the beam wander phenomena [13].

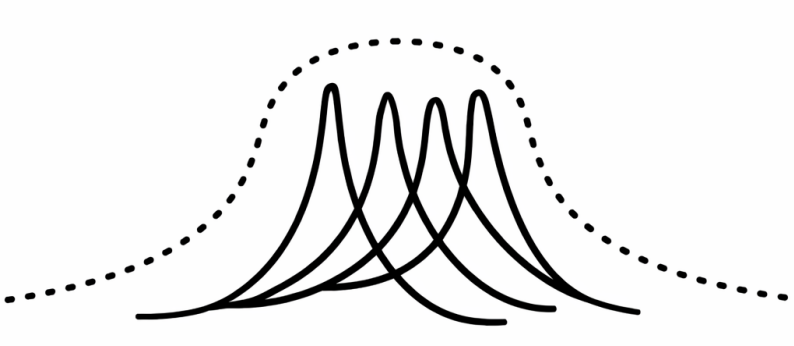


Figure 5 – Beam wander described by movement of the center optical beam, reproduced from [13].

This phenomenon can be characterized statistically by the variance of the light beam center displacement along the axis plane or similarly to a random tilt angle at the

transmitter. Therefore, Eq. [5] emphasizes the close connection between beam wander in the RX plane and the tilt angle variance for a collimated beam,

$$< r_c^2 >= 2.42 C_n^2 L^3 W_0^{-1/3}, \tag{5}$$

where L is the propagation path length in meters, W_0 is the beam radius at transmitter and r_c the radius beam displacement at the receiver.

The latter expression is particularly important because it enables the estimation of the turbulence strength parameter C_n^2 from measurable beam wander statistics once an FSO link is deployed. As such, it provides a practical tool for characterizing the AT-channel and for assessing its impact on pointing stability and overall link performance, thereby supporting the design and validation of turbulence-aware mitigation strategies in FSO communication systems.

Scintillation is another detrimental effect in FSO communication systems, which causes signal fading and in severe cases, can lead to temporary link outages. In FSO links, scintillation manifests as random variations in the received optical intensity caused by constructive and destructive interference of the distorted wavefront. These fluctuations directly affect key performance metrics, including the SNR, bit error rate (BER), and link availability.

To quantitatively assess the scintillation severity, the scintillation index (σ_I^2) is commonly employed and is defined as the normalized variance of the received irradiance and can be expressed as shown in Eq. [6],

$$\sigma_I^2(R, Z) = \frac{\langle I^2(R, Z) \rangle}{\langle I(R, Z) \rangle^2} - 1, \tag{6}$$

where $I(R, Z)$ denotes the irradiance at a position R after propagating over a distance Z, and $\langle \cdot \rangle$ represents ensemble averaging. The scintillation index provides a direct measure of turbulence-induced fading and is therefore a fundamental parameter for predicting FSO system performance.

Under weak-to-moderate turbulence conditions, scintillation can be related to the Rytov variance (σ_R^2), given by Eq. [7],

$$\sigma_I^2 = \sigma_R^2 = 1.23\, C_n^2\, k^{7/6} Z^{11/6}, \tag{7}$$

where C_n^2 is the refractive-index structure parameter, k is the optical wave number, and Z

is the propagation distance.

Based on the value of σ_R^2, turbulence regimes are commonly classified as weak ($\sigma_R^2 < 1$), moderate ($\sigma_R^2 \approx 1$), strong ($\sigma_R^2 > 1$), and saturation regimes ($\sigma_R^2 \gg 1$). While the scintillation index captures the average strength of irradiance fluctuations, it does not fully describe their statistical behavior. A complete characterization of turbulence-induced fading therefore requires modeling the probability density function (PDF) of the received irradiance. Such statistical descriptions are essential for accurate channel modeling, performance analysis, and the design of robust mitigation techniques. Consequently, the next section focuses on the statistical modeling of irradiance scintillation and the corresponding PDFs used to represent the optical wireless channel under different turbulence regimes.

2.4- Channel irradiance modeling

To design, implement, and operate efficient optical communication systems, it is essential to understand the fading characteristics of the AT-channel. In outdoor environments, the atmospheric channel exhibits a random and dynamically varying nature. The propagation path of the optical beam fluctuates at rates on the order of kilohertz, which poses significant challenges for real-time data processing and for actuator systems that must respond at comparable speeds. Consequently, the AT channel must be treated as a stochastic process, considering its cumulative effects over time. In this context, probability density functions (PDFs) are employed to model the optical power received in FSO systems statistically [14].

The optical power received, often expressed as irradiance, is subject to random fluctuations in the refractive index of the propagation medium. Accordingly, it is well established that PDFs such as the lognormal, Gamma, Rician and Gamma-Gamma distributions have been traditionally employed to characterize normalized irradiance (NI) fluctuations in FSO channels [14]. While the lognormal model accurately describes weak turbulence regimes, it becomes inadequate under moderate-to-strong scintillation conditions. The Rician distribution is suitable for scenarios in which a dominant line-of-sight optical component coexists with scattered contributions, capturing partially coherent or aperture-averaged propagation effects. However, for moderate-to-strong turbulence, the

Gamma–Gamma distribution provides a more comprehensive statistical representation, as it models both small-scale and large-scale irradiance fluctuations, offering accurate fitting over a broader range of atmospheric conditions.

A more detailed analysis reveals that, in early studies on irradiance statistics, researchers relied on single-family distributions, most notably the lognormal model. However, later theoretical and experimental investigations demonstrated that optical turbulence exhibits a composite and nonstationary behavior along the propagation path, preventing accurate characterization by a single statistical law [13]. This motivated the development of more general models capable of describing irradiance fluctuations over arbitrary turbulence strengths.

In this context, model validation depends strongly on the availability and representativeness of measured fading samples. Limited datasets lead to empirical probability density functions that are sensitive to histogram resolution and bin selection, potentially biasing the estimation of channel statistics [14]. Therefore, the choice of distribution must consider both the physical propagation regime and the statistical robustness of the observed data.

A theoretical breakthrough emerged from the extended Rytov formulation, in which irradiance fluctuations are represented as a doubly stochastic process [14]. Under this framework, large-scale and small-scale turbulence effects are modeled as independent Gamma random processes whose product leads to the Gamma–Gamma distribution, now widely adopted for describing turbulence-induced fading in optical wireless channels.

2.4.1 Lognormal model

When describing irradiance PDFs under weak turbulence, wave depolarization is negligible [14]. The position vector will henceforth denoted by R and its electric field ($\vec{E}$), spatially represented by $E(R)$ for convenience. The Gaussian complex variable $\Psi(R)$ defined as the natural logarithm of the propagating field $E(R)$ and is termed the Rytov transformation expressed in Eq. [8], as follows,

$$\Psi(r) = \ln\big[E(R)\big], \tag{8}$$

where the complex electric field and its free-space with turbulence and in the absence

(without turbulence, $E_0(R)$) are by definition given as Eq. [9] and Eq. [10], respectively,

$$E(R) = A(R)\exp\big(i\phi(R)\big), \tag{9}$$

and,

$$E_0(R) = A_0(R)\exp\big(i\,\phi_0(R)\big) \tag{10}$$

where $A(R)$, $\phi(R)$, and $A_0(R)$, $\phi_0(R)$ represent the amplitude and phase of the actual field with and without AT, respectively.

To derive the irradiance statistics, we combine Eq. [8] with Eqs. [9] and [10] yielding the turbulence-induced field amplitude fluctuation given is,

$$\Psi(R) = \ln\left[\frac{A(R)}{A_0(R)}\right] + i\big[\phi(R) - \phi_0(R)\big] = X + iS. \tag{11}$$

Thus, assuming that $\Psi(R)$ is Gaussian, it follows that X is Gaussian distributed log-amplitude fluctuation, and similarly S is Gaussian distributed phase fluctuation of the field. By concentrating only on the field amplitude, however, the PDF of X is thus represented in Eq. [12],

$$p(x) = \frac{1}{\sqrt{2\pi\sigma_R^2}}\exp\left\{-\frac{\big(x - \mathbb{E}[X]\big)^2}{2\sigma_R^2}\right\}, \tag{12}$$

where $\mathbb{E}[X]$ denotes the expectation of X and σ_R^2 is the log-amplitude variance, commonly referred to as the Rytov parameter. The Rytov parameter (σ_R^2) typically characterizes the variation of field amplitude within the AT scenario and is related to the index of refraction fluctuations.

The field irradiance (intensity) in the turbulent medium is $I_t = |A(R)|^2$, while the intensity in free-space (no turbulence) is given by Eq. [13],

$$I_0 = |A_0\,(R)|^2\,. \tag{13}$$

And the log intensity is then given by Eq.[14],

$$l = \log_e\left|\frac{A(R)}{A_0(R)}\right|^2 = 2X. \tag{14}$$

Hence, becomes Eq. [15],

$$I_t = I_0 \exp(l). \tag{15}$$

To obtain the irradiance PDF, invoke the transformation of the variable, $p(I) = p\left(X\right)\left|\frac{dx}{dl}\right|$, to arrive at the log-normal distribution function given by Eq.[16],

$$p(I) = \frac{1}{\sqrt{2\pi}\sigma_l}\frac{1}{I}\exp\left\{-\frac{\left(\ln\left(I/I_0\right) - E\left[l\right]\right)^2}{2\sigma_l^2}\right\} \quad I \geq 0 \tag{16}$$

In the region of weak fluctuations, the statistics of the irradiance fluctuations have been experimentally shown to follow the log-normal distribution. The log-intensity variance $\sigma_l^2 = 4\sigma_R^2$ and the mean log intensity $E[l] = 2E[X]$. Following that $E[\exp(l)] = E\left[I/I_0\right] = 1$ since there is no energy loss during the turbulence-induced scattering process. The expectation $E[l]$ is obtained for any real-valued Gaussian random variable [14]. The Fig. 6 shows distinct log-normal PDFs with $(E[l] = 0)$ and different variance values.

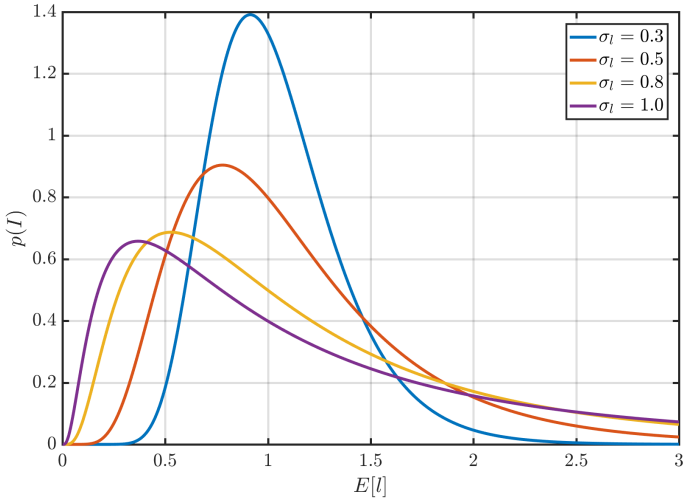


Figure 6 – Log-normal PDF with $E[l] = 0$ and for a range of variance values.

2.4.2 Gamma model

In probability theory and statistics, the Gamma distribution is a versatile two-parameter family of continuous probability distributions. It plays a fundamental role in modeling a wide variety of phenomena due to its flexible shape, which can describe different types of data behavior. Notably, the Gamma distribution generalizes several important distributions, including the exponential and chi-squared distributions, as special cases.

The distribution is characterized by its shape parameter α and an inverse scale parameter $\lambda = \frac{1}{\theta}$, often called the rate parameter. A random variable X that follows a Gamma distribution with shape α and rate λ is denoted by Eq.[17],

$$X \sim \Gamma(\alpha, \lambda). \tag{17}$$

The PDF for the shape-rate parameterization is given by Eq. [18],

$$f(x; \alpha, \lambda) = \frac{\lambda^{\alpha} x^{\alpha-1} e^{-\lambda x}}{\Gamma(\alpha)}, \quad x > 0, \quad \alpha, \lambda > 0, \tag{18}$$

where $\Gamma(\alpha)$ is the Gamma function. For all positive integers α, the Gamma function satisfies $\Gamma(\alpha) = (\alpha - 1)!$. The Gamma distributions mathematical properties, including its mean, variance, skewness, and higher moments, provide a rich framework for statistical analysis and inference. The Fig. 7 shown distincts Gamma PDFs with mode=1 and for differents variace values.

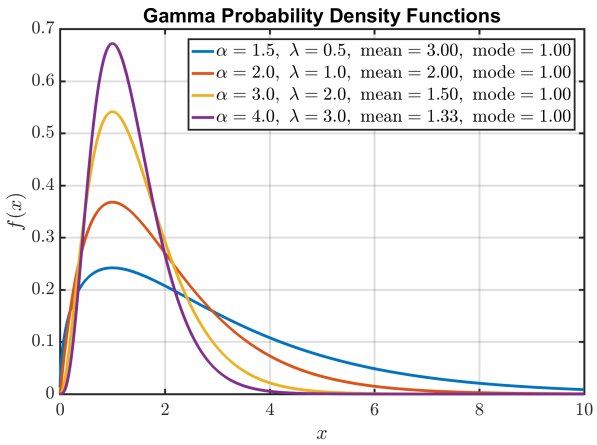


Figure 7 – Gamma probability density function with mode=1 and for a range of variance.

Despite the usefulness of such statistical models, the AT-channel remains inherently random, nonstationary, and highly sensitive to environmental conditions changes. The transition from theoretical modeling to practical deployment therefore exposes significant challenges. Owing to the stochastic nature and limited predictability of the AT channel, purely analytical approaches become increasingly inadequate, specially under strong turbulence conditions. As a result, contemporary FSO systems have progressively relied on data-driven strategies, where ML techniques emerge as powerful tools to learn channel behavior, enable adaptive compensation, and enhance physical-layer resilience. This motivates the investigation of ML-assisted control and mitigation mechanisms, which constitute a central focus of the subsequent sections of this thesis.

2.5- Machine learning algorithms

Machine Learning refers to computational methods that learn a task from data.. In the case of supervised learning, the training data consist of pairs of input vectors and desired outputs. The output can be a continuous value for the case of regression. The task of the supervised learner is to predict the value of the function for any valid input object after having seen several training examples, i.e., pairs of input and target output. Therefore, for the task of ML prediction used in this thesis to predict AT-behavior, the artificial neural networks multilayer perceptrons (ANN), CNN, linear regression (LR), and k-nearest neighbors (KNN) are briefly explained as follows.

2.5.1 Artificial neural networks

Artificial Neural Network emerged in the 1940s and refers to a computational algorithms inspired by biological neurons behavior. Among the various architectures, the most widely adopted are the feedforward networks, in which nonlinear elements (neurons) arranged in layers construct a hyperplane for regression tasks [15, 16]. Figure 8 illustrates the topology of the multilayer perceptron.

In Figure 8, the input signals (x_i) associated with each neuron, which represent

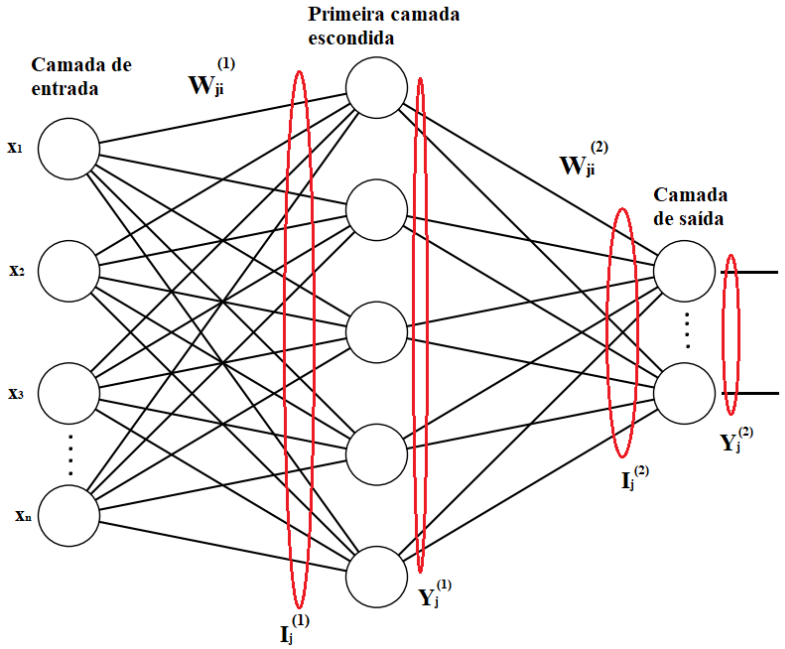


Figure 8 – Topology of an artificial neural network [17].

information provided from the FSO sensor system, and are weighted by the synaptic weights (W_{ji}) connecting the input i to neuron j. The input value to each neuron (j) in the first hidden layer can be modeled by Eq. [19],

$$I_j = \sum_{i=1}^{N} W_{ji}\, x_i. \tag{19}$$

Each neuron receives the input signal and processes it to produce an excitatory or inhibitory response to the neurons of the subsequent layer. The processing itself is performed by the network activation function $g(\cdot)$, commonly implemented as a hyperbolic tangent or logistic function in multilayer perceptron type networks. The output of the neurons in the first layer can thus be expressed as in Eq. [20],

$$Y_j = g(I_j). \tag{20}$$

Hence, the output of the final layer represents the prediction output for the FSO controller system. However, before predict can be achieved, the network must undergo a training process to map the input–output relationship. Mathematically, the network seeks

to minimize the cost function defined in Eq. [21],

$$E(k) = \frac{1}{2}\sum_{j=1}^{K}(d_j(k) - Y_j(k))^2, \tag{21}$$

where $d_j(k)$ denotes the desired output of neuron j for the k-th training sample.

The objective of the ANN training process is to adjust the synaptic weight matrix so as to minimize the mean squared error between the actual and desired outputs, according to the weight-update rule in Eq. [22],

$$W_{ji}(t+1) = W_{ji}(t) + \eta\,\delta_j\,Y_i, \tag{22}$$

where W_{ji} is the weight connecting the j-th neuron to the i-th input, η is the learning rate (typically within the range [0.1, 0.9]), δ_j is the local gradient defined by Eq. [23], and Y_i denotes the i-th input,

$$\delta_j = (d_j - Y_j)\,g'(I_j), \tag{23}$$

Consequently, in each layer, the weights are iteratively adjusted to minimize the overall error, namely backpropagation [18].

In this thesis, ANNs were used in conjunction with optical-power triangulation technique in experiment 1, where the optical power sensed by phototransistors displaced in a triangular shape function as inputs for the ANN presented.

2.5.2 Convolutional neural networks

Convolutional Neural Networks (CNNs) are specifically designed to process spatially structured data, such as grayscale images acquired by CCD cameras, by learning two-dimensional feature representations through backpropagation. CNN architectures are composed of successive mathematical operations, including convolutional, pooling, and fully connected layers, which collectively enable hierarchical feature extraction.

As illustrated in Fig. 12, grayscale image data are represented as a two-dimensional matrix. The convolution operation is performed by a kernel, defined as a small matrix that slides across the image by performing element-wise multiplications and then summing the

results. This process allows the network to extract local spatial features, such as edges, gradients, and textures, which are subsequently combined in deeper layers to form more abstract representations.

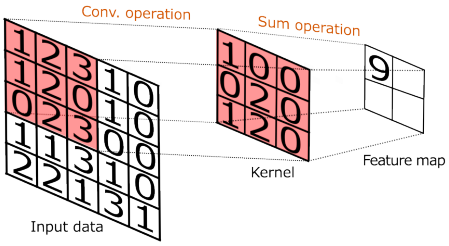


Figure 9 – The kernel starts at the top-left corner of the input data.

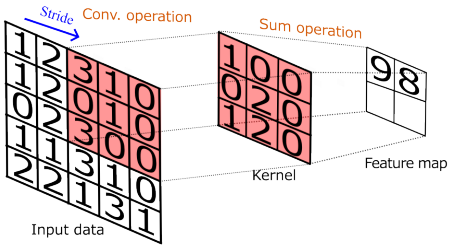


Figure 10 – The kernel moves across the input according to the defined stride.

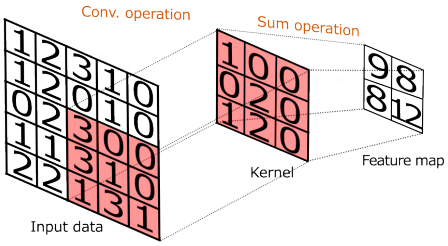


Figure 11 – The kernel completes the convolution operation after scanning the entire input.

Figure 12 – Example of convolution operation with a kernel size of 3×3, no padding, and a stride of 2.

The kernel is applied across the input data, and the multiplication operation between each element of the kernel and data is calculated and summed up to obtain the output value for each corresponded index of the output data, called a feature map. The output of the convolution operation is called feature map and represents the extracted information from the input data. This procedure can be repeated by applying multiple kernels, also known as depth, to enable the extraction of distinct features from the initial input image. In fact, four hyperparameters define the convolution operation, which are the size of kernel grid ($N \times N$), number of distinct kernels (depth), padding and stride. The padding is the process of adding extra pixels around the border of an input image before applying a convolutional layer. This is typically done to control the spatial dimensions of the output feature map and to preserve the information at the edges of the input. The stride defines the distance between two successive positions in the kernel grid, which directly impacts the size of the output of the feature map. Thus, after the convolution operation,

the max-pooling layer shown in Fig. 16 is important to condense the information from the feature maps and perform a reduction of feature map dimensions to decrease the number of neurons in subsequent layers and to reduce feature-map dimensions and improve computational efficiency during training and inference. In summary, the max-pooling layer is a matrix grid that overlaps with the feature map and extracts the maximum value within each patch.

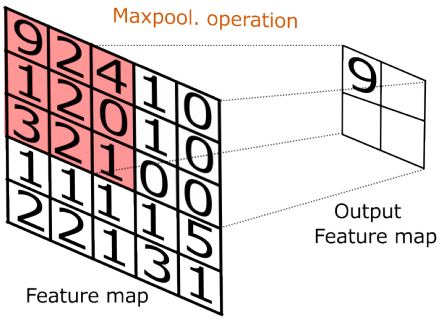


Figure 13 – The pooling kernel starts at the top-left region of the feature map.

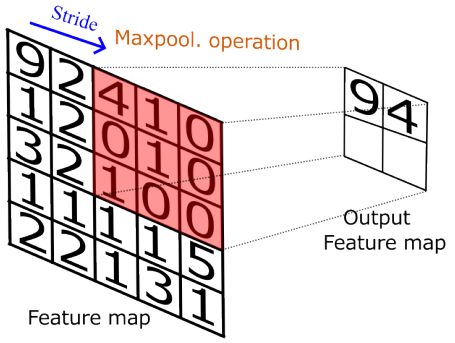


Figure 14 – The kernel slides across the feature map according to the stride, selecting the maximum value within each region.

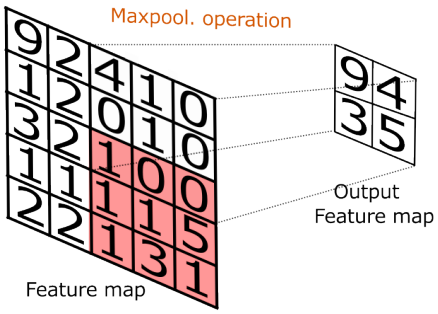


Figure 15 – The pooling operation completes after covering the entire feature map, resulting in a spatially reduced representation.

Figure 16 – Example of max-polling operation with a kernel size of 3×3, no padding, and a stride of 2.

The output size of the feature maps for both convolution and max-pooling layers can be calculated when using squared grid size, i.e., same size for rows and columns, using the Eq. [24],

$$N_{out} = \frac{I_{input} - (N_k + 2\,N_P)}{N_S} + 1, \tag{24}$$

where the N_{out} represents the output feature map size, N_k is the kernel grid size, N_P is the size of the padding and N_S is the stride.

In general, the CNN architecture was adopted for processing two-dimensional images data captured by CCD cameras. Thus, in this thesis, a CNN model was employed for AT and PEC in both experiments 2 and 3.

2.5.3 Linear regression

LR is a fundamental supervised learning technique that models the relationship between one or more independent variables and a dependent variable by fitting a linear function to the data. The primary objective of LR is to minimize the residual sum of squares between the observed values and the predicted outputs. This optimization process is typically achieved through the least squares method, as formulated in Eq. [25],

$$f(x, y) = (x^T y + c)^d, \tag{25}$$

where x represents the vector of input features, y denotes the corresponding model coefficients, c is the bias term, and d indicates the polynomial degree of the model. In this work, a first-degree polynomial ($d = 1$) was adopted, corresponding to the standard linear regression case [19].

By constraining $d = 1$, the model assumes a linear dependency between the predictor variables and the response, simplifying the interpretation of feature influence. The coefficients are estimated by minimizing the cost function, expressed as the mean squared error (MSE) between predicted and actual outputs. Despite its simplicity, LR serves as an effective baseline model, providing a clear benchmark for evaluating the performance improvements achieved by more complex architectures. Indeed, In this work, LR was applied in conjunction with optical-power triangulation technique, where the optical power sensed by phototransistors displaced in a triangular shape function as inputs for the LR presented.

2.5.4 K-nearest neighbors

The K-Nearest Neighbors (KNN) regression algorithm is a non-parametric method that estimates the output of a query sample by analyzing its proximity to the k-closest samples in the training dataset. Instead of learning an explicit mapping function, KNN relies entirely on instance-based learning, where predictions are computed based on local similarity measures.

In this thesis, the Euclidean distance are computed between the test sample and all training samples is calculated to determine the k-nearest neighbors. The final predicted value is then obtained as the weighted average of the neighbors' outputs, where the contribution of each neighbor is inversely proportional to its distance from the query point. Formally, this can be expressed as shown in Eq. [26],

$$\hat{y}(x) = \frac{\sum_{i=1}^{k} w_i \, y_i}{\sum_{i=1}^{k} w_i}, \tag{26}$$

where y_i represents the target values of the k-nearest samples and $w_i = 1/d(x, x_i)$ denotes the weight associated with each neighbor, based on the Euclidean distance $d(x, x_i)$.

The parameter k is commonly empirically tested during the training/validation stage. The weighting mechanism ensures that closer samples exert a greater influence on the output, thereby enhancing prediction accuracy. Due to its simplicity and non-parametric nature, KNN regression is particularly suitable for small to moderately sized datasets. However, the KNN major drawback is the increase in the dataset, leading to time consumption for Euclidean distance calculation for every pair of data. Similarly to ANN and LR, KNN was also used in combination with optical-power triangulation, where the optical power sensed by phototransistors displaced in a triangular shape function as inputs for the KNN presented in this section.

Although statistical channel models and ML techniques provide valuable insight into the behavior of AT, their ultimate relevance depends on practical validation under realistic propagation conditions and its integration with electro-electronic devices typically used within FSO communication links, for instance, Gimbals, Fast-steering mirrors (FSM) and Spatial Light modulators (SLM). Consequently, the deployment of adaptive and data-driven mitigation strategies requires careful integration with physical optical devices and control systems. In this context, experimental testbeds play a fundamental role in assessing the

feasibility, robustness, and performance of ML-assisted FSO techniques. By implementing closed-loop control schemes directly on electro-optical hardware, it becomes possible to evaluate how learning-based algorithms interact with atmospheric impairments such as scintillation, beam wander, and PE in realistic scenarios. These experimental assets enable not only performance benchmarking but also the identification of practical limitations and future research directions for the research community.

2.6- Literature review of tracking, pointing error and wavefront-compensation methods

Regarding the feasibility and reliability of FSO links, a critical requirement is precise point-to-point alignment of the transceivers. To achieve functional steering, it is necessary to implement an ATP mechanism [20]. To address this challenge, researchers have developed techniques based on feedback systems. Following an initial coarse alignment, i.e., approximate steering, the transceivers exchange information about beam steering quality. In this context, semiconductor-based electronics are employed to detect beam deviation at the receiver end and, using feedback, request realignment from the transmitter. For instance, S. Muta et al. [21] used rectangular photodiodes to monitor beam movements and Ethernet protocol-based cabled feedback to control receiver realignment mounted on servomotors. Although effective for maintaining coarse alignment, this method lacked the precision required for advanced applications, such as direct FSO-to-fiber coupling.

Aiming to optimize the time-consuming feedback task, retroreflective components have been employed to reflect the beam-deflecting information and thus reuse the wireless channel. For example, Liu et al. [23] used reflective surfaces to return part of the beam for analysis, enabling tighter control. However, in this feedback method, the beam carrier senses the atmospheric turbulence increase due to doubled propagation paths. Following, M. Matsumoto et al. [24] similarly implemented the beam displacement sensing and tracking directly at the RX using a quadrant photodetector (QPD) and PID-based to control a movable receiver plane. While this approach demonstrated improved control performance, the reliance on QPD-based solutions can significantly increase capital expenditures, posing economic barriers for new market entrants.

Exploiting advancements in ML algorithms, R. Bazil [25] employed a QPD combined with an ANN to automate an FSM for beam tracking and steering. In fact, several ML models have demonstrated potential in diverse FSO applications, including channel estimation, jitter compensation, modulation classification, underwater communications, AT-wavefront correction, and orbital-angular-momentum (OAM) demodulation [26, 27]. Researchers have increasingly exploited the intrinsic properties of light to perform data processing directly in the optical domain, rather than exclusively in the electronic domain, thereby reducing latency. These photonic-computing-based ML architectures include on-chip optical neural networks integrated into photonic circuits as well as non-chip-integrated Diffractive Deep Neural Networks (D2NN) [28–30].

The coarse alignment can also take advantage of the multiplexing of different beam carriers. This means that a specific wavelength can be employed for data, and a different one for the beam steering control. Indeed, the use of commercial cameras for visible light addresses the constraints of limited budgets and practical implementations, while filtering only the visible light and neglecting the data source commonly in the infrared (IR) or ultraviolet (UV) range. In this context, A. Campos et al. [31], proposed computer vision (CV) using a CMOS camera to sense beam deviation and feedback compensation commands to the TX for an initial alignment of the transceivers. While it is effective for coarse alignment, the CV-based method is time-consuming due to the computational complexity of the algorithms involved, which presents an increased overhead.

Keeping the cost-related constraints and avoiding relying on off-the-shelf commercial solutions, some studies in the literature have explored simple approaches using phototransistors arranged in geometric configurations to detect beam deflection. Notably, V. Silva et al. [32] proposed a low-cost solution based on a triangulation scheme using phototransistors. While the latter approach demonstrated potential, its performance was limited by computational overhead introduced by the use of an iterative equation system (EQS), which impacted the time elapsed for predicting the beam tracking. The related works have reported the use of ATP schemes. However, as previously mentioned, these systems often operate only for coarse alignment. In FSO-to-fiber coupling applications, the presence of severe AT channels, combined with additional disturbances such as strong wind loads that induce mechanical oscillations, demands finer LOS tuning to maintain stable alignment.

To overcome these issues, SLMs, a pixelated devices capable of digitally controlling

the refractive index of each pixel, have been tested for controlled small-angle beam deflection to enhance FSO-to-fiber steering. Niu et al. [33], for instance, employed a CCD camera at the RX to provide beam centroid displacement feedback and generated blazed gratings on the SLM for diffraction-based PE compensation. Similarly, Spaander et al. [34] combined a phase ramp grating with a Fresnel lens loaded onto the SLM to compensate for mechanically induced PE via beam diffraction, while Goto et al. [35] utilized gratings and SLMs to displace the optical beam and enable switching into a multi-core fiber. However, the use of gratings in combination with SLMs introduces undesired diffraction patterns that deviate from the ideal calculated response, primarily due to SLM pixel voltage leakage and the scattering of optical power into multiple diffraction orders caused by the intrinsic nature of gratings.

In addition to these issues related to grating-based approaches, the AT channel update rate also represents a significant limitation. Even the reported use of SLMs controlled by non-analytical algorithms, such as SGD or GS method requires multiple iterations, leading to substantial computational overhead and reducing their applicability in FSO communication systems [34, 36]. Although effective, these approaches impose heavy computational demands, rendering them impractical for channels that fluctuate on the order of kilohertz. These impairments can, however, be mitigated through the use of ML models, such as feedforward CNNs, As demonstrated in the literature [15], ML models can provide faster predictions than iterative methods.

In general, the PEs induced by AT channels or mechanical instabilities can be mitigated by the aforementioned techniques. Nevertheless, these systems typically assume the existence of a preceding AT wavefront compensation stage. In other words, the propagation medium introduces wavefront distortions due to refractive index inhomogeneities, leading to power fading and scintillation at the receiver, which degrade link reliability and BER performance

To address AT-induced wavefront distortions, SLMs have been experimentally tested in combination with various autonomous control algorithms. For instance, P. Chen et al. [37] employed an SLM with an iterative SGD method for AT wavefront compensation. Similarly, H. Chang et al. [38] utilized an SLM together with the GS algorithm to compensate AT-disrupted OAM beams. However, these techniques require derivative computations and fast Fourier transforms (FFTs), and are inherently iterative, resulting in significant computational overhead. This limits their applicability to real-time FSO systems when

compared with ML models approaches such as the CNN. Following this approach, W. Xiong et al. [39] used SLMs to emulate AT effects by loading phase masks, while a secondary device applied compensation masks predicted by a CNN to mitigate the induced turbulence in vortex (VB) and Laguerre–Gaussian (LG) beams.

These contributions delineate a central focus of this thesis, namely the interaction between the optical carrier and its propagation medium and consequently the turbulent atmosphere, while simultaneously reflecting the broader challenges faced by the telecommunications field in rendering FSO systems practically feasible. Building on these challenges, this doctoral thesis seeks to demonstrate the feasibility of combining ML techniques with optical devices to enable highly reliable FSO links. The research emphasizes experimental validation, addressing both the design of the physical layer through the implementation of ATP mechanisms and the mitigation of atmospheric turbulence effects, such as wavefront distortions and pointing errors. In doing so, this work contributes to the academic community by providing practical results and insights that advance the understanding and overcoming of AT and technological limitations in FSO systems.

To provide a better guindance and contextualization about the contributions of this work within the broader landscape of FSO impairment mitigation, Tables **??** provide comprehensive comparisons with prior approaches reported in the literature for each respective experiment. These tables highlight the different approaches by the literature referenced in this thesis.

Table 2 – Comparative analysis of beam tracking techniques for Experiment 1.

Reference	Sensor	Controller	Key Limitations
Muta et al. [21]	Rectangular photodiodes	PID	Coarse alignment only; not suitable for fiber-coupling applications.
Malak et al. [22]	Corner cube and QPD	PID	Double path length; increased turbulence exposure.
Liu et al. [23]	Retro-reflective tape and QPD	MEMS control	Double-path turbulence; complex optical design.
Campos et al. [31]	CMOS camera	Computer Vision	Coarse alignment only; high computational overhead.
Raj [39]	QPD	ANN	Relies on costly QPD components.
Silva et al. [32]	Optical power triangulation	Iterative Solver (EQS)	Needs pre-compensated GB; high computational cost (340 ms); noise sensitive; limited range (12 mm).
This work [8]	**Optical power triangulation with low-cost PTs**	**ANN, LR, KNN**	**Needs pre-compensated GB;**

Note: QPD = Quadrant Photodetector, PT = Phototransistor, EQS = Iterative Equation System.

Table 3 – Comparative analysis of wavefront compensation for Experiment 2.

Reference	Control Algorithm	Key Limitations
Chen et al. [37]	SGD	Iterative; derivative computations required; high computational overhead.
Chang et al. [38]	GS	Iterative; requires FFT computations; significant computational overhead.
Xiong et al. [39]	CNN	Needs training dataset for CNN deployment.
Hu et al. [40]	Blazed gratings / Phase ramps	Diffraction losses; multiple orders; power scattering; limited efficiency.
This work [9]	**CNN**	**SLM refresh rate limited (1 Hz); geometric losses.**

Table 4 – Comparative analysis of pointing error compensation for Experiment 3.

Reference	**Control Algorithm**	**Key Limitations**	
Niu et al. [33]	Blazed gratings	Diffraction-based	Unwanted diffraction orders; power scattering; pixel voltage leakage; deviation from ideal response
Spaander et al. [34]	phase ramp + Fresnel lens	Complex phase pattern design; power scattering; pixel voltage leakage; deviation from ideal response	
Goto et al. [35]	Blazed gratings	Power scattering; pixel voltage leakage; deviation from ideal response	
Chen et al. [37]	SGD	Iterative; multiple iterations required; high computational overhead; slow convergence	
Chang et al. [38]	GS	Iterative; FFT computations; significant overhead;	
This work [10]	**CNN**	**SLM refresh rate limited (1 Hz); Beam narrowing due to diffraction**	

Motivated by these considerations, the following section presents the experimental platforms developed in this thesis. The proposed setups demonstrate the practical implementation of ML-driven techniques for ATP, as well as for AT effects mitigation using, providing a direct link between theoretical modeling and real-world FSO system performance.

All experimental configurations presented herein can be regarded as functional subsystems of a complete ATP architecture. Specifically, experiment 1 introduces a machine-learning-based optical beam tracking approach grounded in the optical power triangulation method, improving both the dynamic range and response time of pointing error sensing. This technique naturally integrates into the tracking subsystem of an FSO link. The experiment 2 addresses atmospheric-turbulence-induced wavefront distortions through SLM-based compensation, which can be interpreted as a front-end correction

stage that enhances the robustness and overall effectiveness of the ATP mechanisms. Finally, experiment 3 investigates the use of an SLM for fine pointing error compensation, enabling high-precision beam control that can be incorporated into the pointing subsystem to maintain reliable LOS alignment.

3- Experiment 1: ML-driven FSO tracking error mitigation

Optical beams propagating through the atmospheric channel are subject to beam wander, which causes random beam displacements and results in PE for FSO links. These effects are further exacerbated by mechanical disturbances, such as building sway and wind-induced vibrations, leading to additional misalignment between transceivers. Consequently, reliable FSO operation critically depends on effective compensation of channel- and platform-induced disturbances and, in particular, on maintaining precise point-to-point alignment [50].

To this end, FSO systems require an ATP mechanism [20]. Most ATP solutions rely on feedback-based control architectures. After an initial coarse alignment, the transceivers exchange information regarding beam alignment quality to refine steering accuracy. Typically, semiconductor-based sensors at the receiver detect beam deviations and, through a feedback loop, command realignment at the transmitter. For example, S. Muta et al. [21] employed rectangular photodiodes to monitor beam motion and used ethernet-based feedback to control servomotor-mounted optics. While effective for coarse alignment, such approaches lack the precision required for demanding applications, such as direct FSO-to-fiber coupling. To reduce feedback latency, several studies have employed retroreflective components. For example, Malak et al. [22] and Liu et al. [23] used reflective surfaces to return part of the beam for analysis, enabling tighter control. However, in this feedback method, the beam carrier senses the AT increase due to doubled round-trip propagation. Subsequently, M. Matsumoto et al. [24] and A. Bekkali et al. [51] implemented displacement sensing and tracking directly at the RX using a QPD and a PID-based controller to actuate a movable receiver plane. While this approach demonstrated improved control performance, the reliance on QPD-based solutions can significantly increase capital expenditures, posing economic barriers for new market entrants.

Exploiting advancements in ML algorithms, R. Bazil [25] employed a QPD combined with an ANN to automate an FSM for beam tracking and steering. In fact, several ML models have demonstrated potential in diverse FSO applications, including channel estimation, jitter compensation, modulation classification, underwater communications,

AT-wavefront correction, and OAM demodulation [26, 28–30]. Researchers have increasingly exploited the intrinsic properties of light to perform data processing directly in the optical domain, rather than exclusively in the electronic domain, thereby reducing latency. These photonic-computing-based ML architectures include on-chip optical neural networks integrated into photonic circuits as well as non-chip-integrated D2NN [28, 29].

The coarse alignment can also take advantage of the multiplexing of different beam carriers. This means that a specific wavelength can be employed for data, and a different one for the beam steering control. Indeed, the use of commercial cameras for visible light addresses the constraints of a feasible project and small budget, while filtering only the visible light and neglecting the data source commonly in the IR or UV spectrum range. In this context, A. Campos et al. [31], proposed CV using a CMOS camera to sense beam deviation and feedback compensation commands to the TX for an initial alignment of the transceivers. While it is effective for coarse alignment, the CV-based method is time-consuming due to the computational complexity of the algorithms involved, which presents an increased overhead.

Considering cost constraints and avoiding reliance on off-the-shelf commercial solutions, several studies in the literature have explored simplified approaches based on phototransistors arranged in geometric configurations to detect beam deflection. Notably, V. Silva et al. [32] proposed a low-cost solution based on an optical power triangulation scheme using phototransistors. While this approach demonstrated promising potential, its performance was limited by the computational overhead introduced by the use of an iterative EQS, which increased the time required to predict beam displacement during tracking.

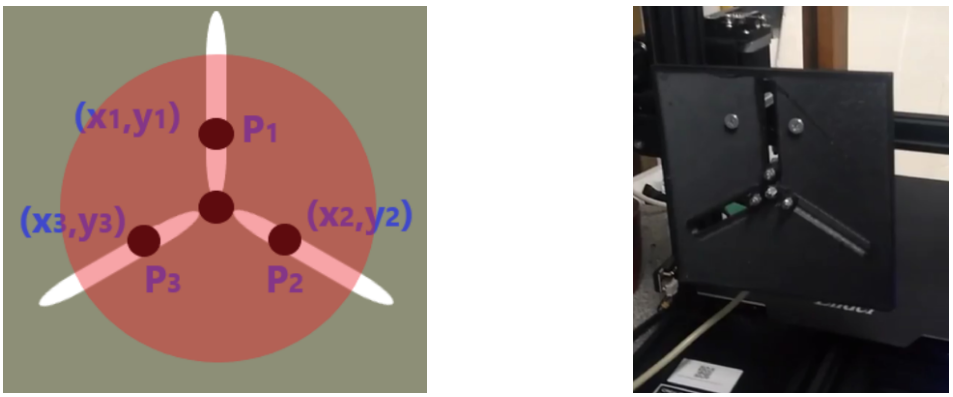
The related previous works have reported the use of ATP schemes. However, in FSO-to-fiber coupling applications, the presence of severe AT, combined with additional disturbances such as strong wind loads that induce mechanical oscillations, demands more refined LOS tuning to maintain stable alignment. To address these impairments the experiment 1 employs an optical power triangulation method with reduced response time, driven by ML algorithms, to track the optical beam at the RX-side. This method, originally introduced in [32], exploits ML techniques, namely ANN, LR, and KNN, to improve tracking accuracy, response time, and dynamic range.

This tracking approach enables the estimation of the Gaussian beam (GB) center displacement, providing a quantitative measure of pointing error for subsequent feedback-

based compensation. The results include a comparative analysis of the proposed ML models and assumes that a preceding AT wavefront compensation stage delivers a quasi-GB to the triangulation method proposed.

3.1- Theory background and methodology

For purposes of tracking the GB with a circular profile, this work employs the optical power triangulation method, first introduced in [32]. The technique uses three PTs, including P_1, P_2, P_3 positioned at the vertices of an equilateral triangle, with side length determined according to the beam width W, as illustrated in Fig. 17.



(a) Receiver plane design. (b) Receiver 3D-printed used in experiments.

Figure 17 – Receiver project design and 3D-printed.

Initial pointing alignment is performed using a fourth PT placed at the center of the triangle. The original method outputs the beam displacement using the Eq. [27],

$$\begin{cases} (x_c - x_1)^2 + (y_c - y_1)^2 - W^2(-\ln \bar{P}_1) = 0 \\ (x_c - x_2)^2 + (y_c - y_2)^2 - W^2(-\ln \bar{P}_2) = 0 \\ (x_c - x_3)^2 + (y_c - y_3)^2 - W^2(-\ln \bar{P}_3) = 0 \end{cases} \tag{27}$$

where $\overline{P_i}$ is the normalized optical power of each PT, the PTs (x_i, y_i) coordinates are known and the beam center displacement represented by (x_c, y_c) are calculated solving simultaneously the EQS.

Therefore, Eq. [27] presents three free variables named x_c, y_c and W, which is the beam-waist at $1/e$. The EQS benchmark run with an average time response of

approximately 340 ms executed using an AMD A4-3305M APU with RadeonHD Graphics (1.90 GHz) and 4 GB of RAM computer.

However, the EQS-based solver is highly sensitive to noise-biased data and lacks adaptability to dynamic scenarios, such as AT conditions. Moreover, its analytical nature makes the approach vulnerable to suboptimal placement of the PTs on the RX plane during installation, introducing offset errors in the beam-tracking process. In this work, the EQS-based method is retained as a benchmark for comparison with the proposed ML-based models.

3.1.1 Experimental FSO system characterization

The experimental setup consisted of a TX comprising a collimated 645 nm light source. The RX was a two-axis movable system mounted on servomotors, equipped with a sensing plane containing the three PTs model PT334-6C, manufactured by Everlight. It is important to note that the PTs were connected to a trimmer potentiometer for voltage output calibration. The signal acquisition was performed using the NI-DAQ model 6216 as a 16-bit data acquisition device, along with a computer for data storage and control operations. The complete system architecture is illustrated in the block diagram shown in Fig. 18.

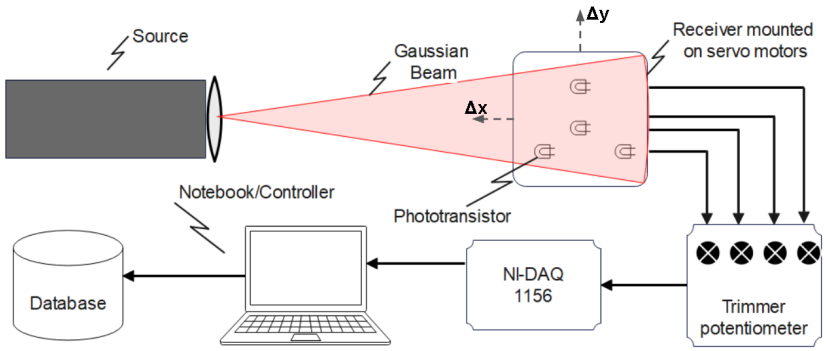
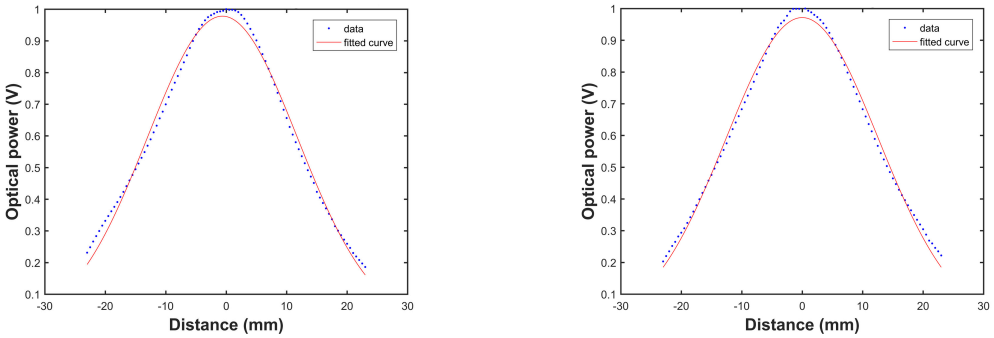


Figure 18 – Experimental setup element devices.

The characterization of the GB was performed by moving the plane on the XY-axis with 1 mm steps collecting 500 samples per point. The beam profile is shown in Fig. 19.

The measured beam width was $W \approx 17.1$ mm, defined as the radius at which the optical intensity falls to $1/e$ of its maximum value at the RX. Table 5 presents the spatial



(a) X-axis profile. (b) Y-axis profile.

Figure 19 – Incident GB characterization with circular profile.

arrangement of the PT_i, where $i = 1, 2, 3$. This configuration satisfies the critical radius condition, $R_{crit} \approx 12.1$ mm, which corresponds to the radial distance associated with the highest derivative of the optical power profile [32].

PT_i	(x , y)
1	(0 , 12.1)
2	(10.5 , -6)
3	(-10.5 , -6)

Table 5 – Cardinal position of the PT_i.

The system's noise sources include thermal noise, residual laboratory light interference, current source fluctuations, and other environmental disturbances. These contributions were lumped into a single noise term for SNR characterization. The SNR was experimentally measured and mathematically modeled based on the radial distance from the GB peak, as shown in Fig. 20.

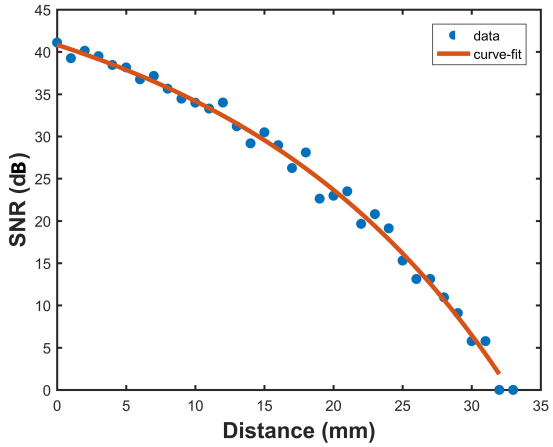


Figure 20 – Average SNR in dB as a function of the radial distance from the GB peak.

After the characterization of the experimental setup, the system was then prepared

for the data acquisition stage required for training the ML-based tracking models.

3.1.2 Data acquisition and transformation

During data acquisition, the impact of different spatial coverage areas on the training data was investigated. Four circular areas with radii (AR) of 0.5, 1, 1.5, and 2 W were used for data collection, as shown in Fig. 21. These varying coverage areas enabled analysis of SNR levels, data diversity, and model accuracy.

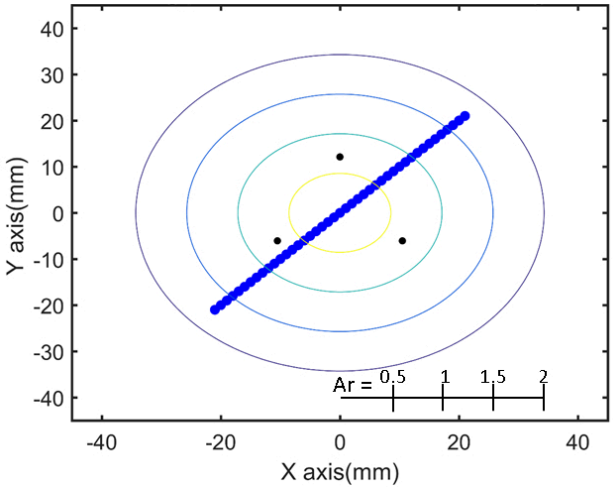


Figure 21 – Areas covered by the different training datasets and the line test data.

The datasets were automatically acquired by randomly moving the RX-plane radially from the center up to the boundary of each AR defined area. This movement of the mobile RX plane was used to emulate the PE induced in real FSO systems by AT or mechanical issues. For smaller AR, samples mainly cover regions near the GB peak, resulting in low variance in the optical power data. Increasing AR expands the sampled area, producing higher-SNR and more diverse data. As shown in Fig. 21, the ML-test dataset is represented by blue dots along the line $y = x$, with a maximum radial distance of about 30 mm, reaching the boundary where noise-induced spurious samples emerge. The study also assessed the impact of dataset size on model performance by acquiring training datasets with 10, 50, and 100 samples per AR.

In fact, given the nonlinear nature of the GBs optical power distribution, a logarithmic transformation was applied to linearize the data, reduce input complexity, and improve model convergence [**?**, **?**]. This also enabled the use of the LR model, which assumes a

linear input-output relationship. Thus, with the transformed dataset available, the selected ML algorithms were trained and subsequently evaluated in terms of response time and accuracy using an independent test dataset.

3.1.3 Machine learning models

Selecting an appropriate ML model usually involves experimental trials and performance evaluation. For the ANN algorithm, the architecture can vary by changing the number of hidden layers and neurons. In this work, ANN models were configured with 3 input neurons, corresponding to the three PTs in the triangulation method, and 2 output neurons representing rectangular coordinates. A single hidden layer with 2, 3, 4, and 5 neurons was evaluated to assess the effect of network complexity on performance. This work assumes the number of hidden neurons to remain lower than twice the number of input neurons [**?**].

In addition to applying a logarithmic transformation, the data are normalized to the range $[-1, 1]$ before being processed by the ANN. The network uses a fully connected feedforward topology with hyperbolic tangent activation functions in the hidden layer. Training is performed via standard backpropagation with batch gradient descent. For prediction tasks like tracking the GB center, where the universal approximation theorem applies, adding more than one hidden layer rarely improves performance and may increase the risk of convergence to local minima [17].

Regarding the LR, this model aims to minimize the residual sum of squares between the observed targets in the dataset. It employs a least squares method to fit a polynomial curve to the training data as shown in Eq. [28],

$$f(x, y) = (x^T y + c)^d, \tag{28}$$

where the parameter d denotes the degree of the polynomial. This work adopted $d = 1$, which intrinsically corresponds to the first-degree polynomial case and therefore the LR [19].

The KNN model stores the entire training dataset and predicts outputs by calculating the Euclidean distance between a test sample and training samples. In this study, $k = 2$ was chosen, so predictions are based on the two nearest neighbors. The output

is weighted by the proximity of these neighbors, with closer samples having a greater influence.

Therefore, after defining the configurations for each ML model, the experimental evaluations were then conducted.

3.2- Results

This section presents the experimental evaluation of the ML algorithms, focusing on prediction accuracy, response time, and robustness to dynamic range variations. The workflow adopted for this analysis is summarized in Fig. 22, which illustrates the sequential steps performed. With the raw experimental dataset, a log-transformation of the data was performed, and an initial investigation was conducted to determine the optimal number of training epochs for the ANNs, with attention to overfitting prevention. Thereafter, the proposed models were trained, and their average performance metrics are reported. Finally, the predictive accuracy of the ANN, LR, and KNN models was evaluated and compared.

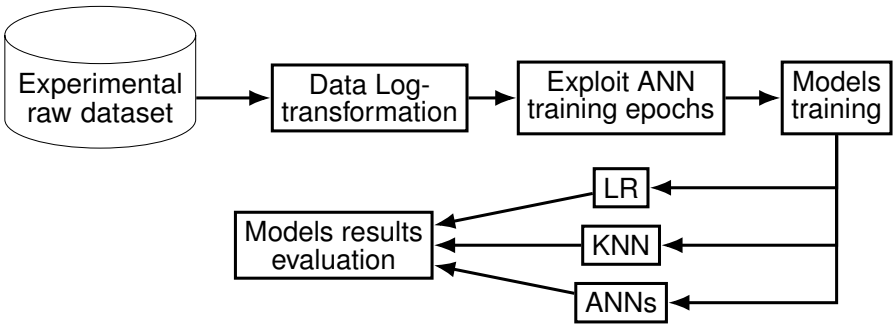


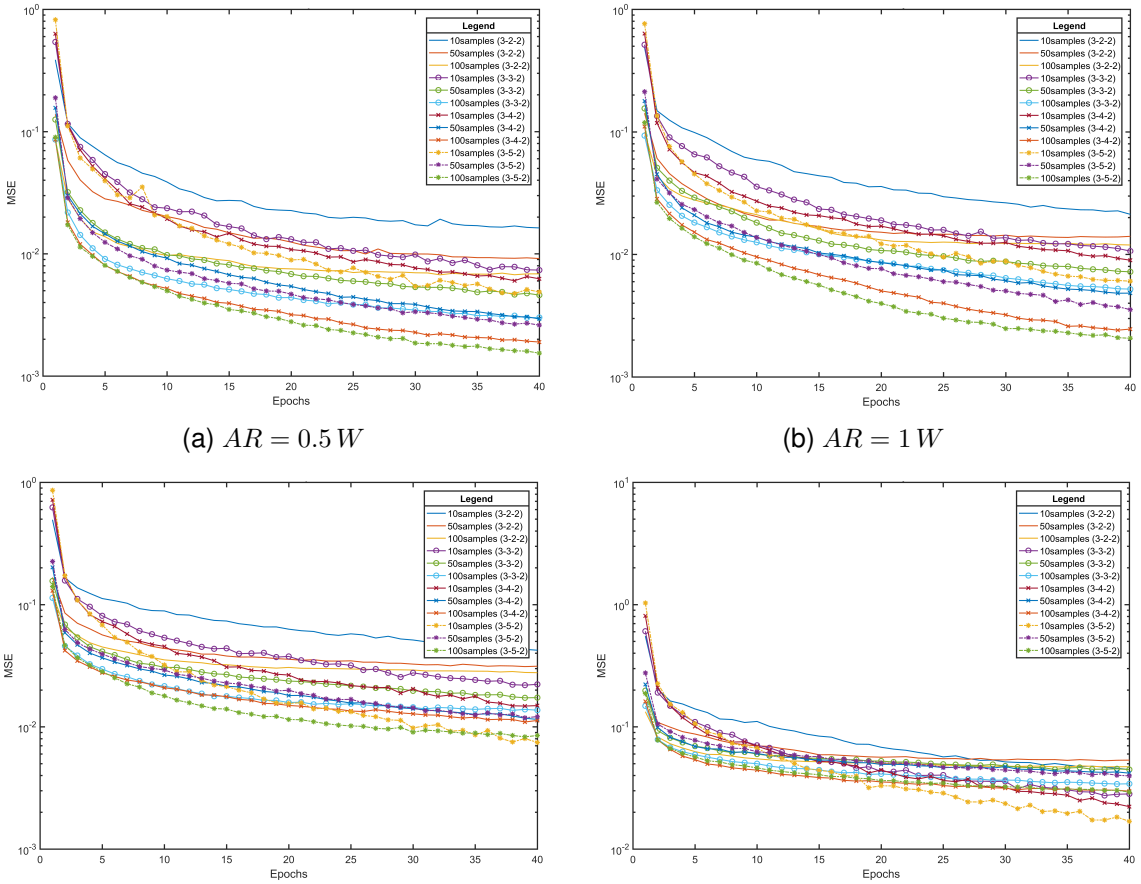
Figure 22 – Block diagram of the proposed methodology.

3.2.1 Tuning the number of ANN training epochs

The effect of varying the training-set size on the ANN's performance was evaluated for each AR considered. The learning rate and momentum were fixed at 0.2 and 0.05, respectively. These values were selected empirically, as preliminary trials indicated they

yielded stable convergence. Altering them would affect the number of epochs required for the training loss to approach its asymptotic value.

The number of epochs required for convergence was first assessed by monitoring the mean squared error (MSE) during gradient descent training, as shown in Fig. 23. Owing to the random initialization of ANN synaptic weights, each topology for each AR was trained independently for 50 runs using subsampling of the original dataset. Training subsets of 10, 50, and 100 samples were randomly drawn to evaluate the effect of training-set size on convergence. Results of the 50 models were averaged to mitigate local minima and underfitting.



(a) $AR = 0.5\,W$ (b) $AR = 1\,W$

(c) $AR = 1.5\,W$ (d) $AR = 2\,W$

Figure 23 – Training loss curves of the multiple ANN configurations, using the MSE loss function, versus the number of epochs for different batch sizes and AR.

As illustrated in the set of plots, multiple ANN topologies were evaluated by varying the number of neurons in the hidden layer from 2 to 5 units. Analysis of these curves reveals that the small weights update variance starts at the 10th epoch onwards. Further training would result in low error reduction per epoch, while increasing computational

overhead. Furthermore, note the loss curve on a log scale, emphasizing the steepest reduction in loss occurring within the first ten epochs, justifying the early stopping criteria adopted to avoid overfitting.

3.2.2 Models accuracy

The influence of dataset size and AR on model accuracy was evaluated to compare the ANN, LR, and KNN models. Model performance was quantified by the mean MSE, computed from the point-to-point Euclidean distance of the line-pattern test data. In contrast to the ANN, the LR and KNN models were trained only once owing to their deterministic approach.

The results in Table 6 indicate several candidate model configurations. Notably, as the trained models AR increased, the prediction error tended to decrease in most cases. Among the well-fitted models, the ANN configurations with 3 and 4 neurons in the hidden layer, trained with 100 samples covering an area of $2\,W$, achieved an average error of 3.3 mm. Another promising configuration was the topology with 5 neurons, trained with 50 samples over an area of $1.5\,W$, yielding an average error of 3.5 mm. This latter model presents the advantage of reducing data acquisition overhead, as it requires fewer samples and minimizes the time needed for RX plane movement during training data collection.

Nevertheless, the 3-neuron model exhibited a lower standard deviation (STD), which indicates that, despite the random weight initialization inherent to ANN training, this configuration consistently produced well-fitted models with reliable accuracy across the multiple SNR conditions present in the line pattern test data. Regarding the LR model, configurations trained with 50 and 100 samples covering an area of $1.5\,W$ achieved an average error of 4.3 mm. Although the model trained with 100 samples exhibited a lower STD, the 50-sample model offers faster deployment due to the reduced number of samples required to achieve similar accuracy. The KNN model achieved an average error of 2.7 mm, representing the lowest value among the models. However, it exhibited a higher STD compared to the ANN, indicating lower robustness for points distant from the center when exposed to spurious data with low SNR. The best-performing models are highlighted in Table 6 to enhance readability.

Approach	Model	N of samples	0.5W		1W		1.5W		2W	
			MSE	STD	MSE	STD	MSE	STD	MSE	STD
		10	11	0.1	8.1	0.29	7.8	0.58	8	1.02
		50	9.1	0.09	5	0.21	3.5	0.09	4	0.14
	3-5-2	100	9	0.23	4.3	0.12	3.6	0.11	3.6	0.17
		10	10.8	0.2	8.2	0.39	7.4	0.37	7.6	0.65
		50	8.8	0.18	4.8	0.09	3.5	0.25	4	0.12
	3-4-2	100	8.8	0.13	4.3	0.11	3.6	0.1	3.3	0.08
		10	11.1	0.4	8	0.26	7.9	0.7	7.6	0.8
		50	8.4	0.24	4.5	0.11	3.5	0.11	4	0.27
	3-3-2	100	8.4	0.27	4	0.16	3.8	0.04	3.3	0.05
		10	10.9	0.4	8.6	0.44	9.5	0.7	9.1	0.7
		50	7.8	0.19	4.3	0.5	4.4	1	4.7	0.4
ANN	3-2-2	100	7.5	0.1	3.9	0.4	4	0.07	3.6	0.7
		10	6.2	0.6	5.3	0.4	5.4	0.8	5.5	1.4
		50	6	0.01	4.8	0.2	4.3	0.4	5.3	0.7
LR	Polynomial degree=1	100	5.9	0.05	4.8	0.05	4.3	0.3	5.6	0.16
		10	11.4	0.5	9.2	0.6	9.3	1.1	7.8	2.1
		50	8.8	0.3	5.8	0.8	3.6	0.52	4.1	0.9
KNN	k=2	100	8.6	0.27	5.5	0.5	2.7	0.25	3	0.4

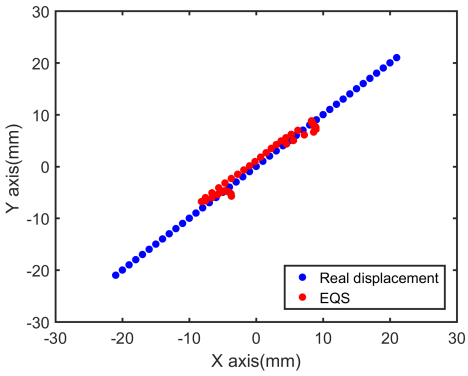
Table 6 – Comparative error metrics MSE and STD of ML models on test dataset.

The tracking performance observations are further validated by the set of plots presented in Fig. 24. Specifically, Figs.18(a) and (c) illustrate the traditional EQS and ML models tracking performance on the line test data, respectively. Additionally, Figs.18(b) and 18(d) depicts the point-to-point Euclidean error of the beam tracking over radial distance from the initial beam center.

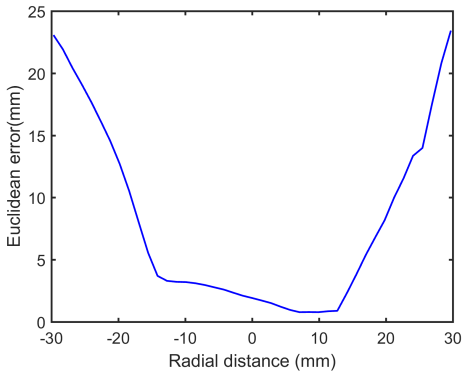
The asymmetrical error observed in the traditional EQS, see Fig. 18(b), may be attributed to suboptimal PT placement on the RX plane, and potentially exacerbated by noise. In contrast, the error sharply increases beyond a radial distance of approximately 12 mm, coinciding with the PTs triangle boundary. The best-performing ML models, highlighted in Table 6, were selected for further evaluation. As shown in Fig. 18(c), the overlapped prediction of the ML models demonstrates the increased tracking dynamic range achieved. Figure 18(d) shows an overall superior performance in the central region, corresponding to samples with higher SNR, with the models being better adapted to the bias caused by the suboptimal positioning of the PTs on the RX plane.

Indeed, Fig. 19(a) illustrates descriptive statistics showing the KNN model outperformed the other models in predicting the GB position within high-SNR data, achieving the lowest minimum error among the evaluated configurations. Conversely, the LR model exhibited the highest maximum and average errors. The ANN models demonstrated robustness to noise and stability by exhibiting an overall lower maximum error value, rather than higher mean accuracy. Statistical significance tests support these conclusions and are further corroborated by Fig. 19(b), which presents the prediction error as a function of SNR, accounting for the radial distance of each data point.

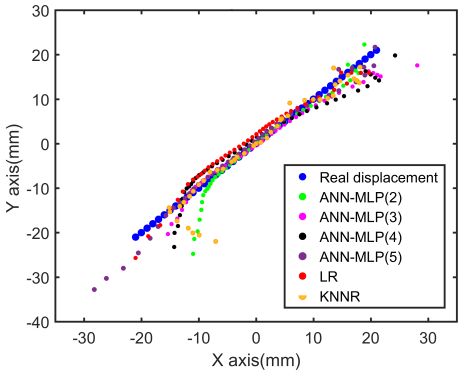
Notably, the ANN models exhibit a quasi-flat error trend across the SNR range



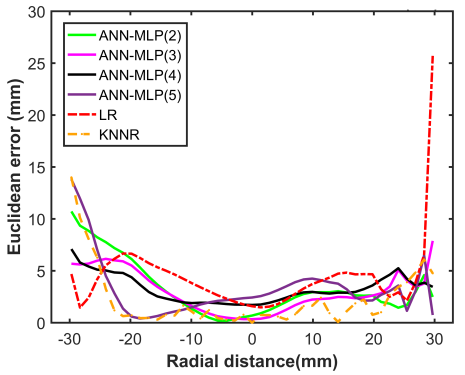
(a) EQS performance over test data.



(b) EQS performance versus radial distance.

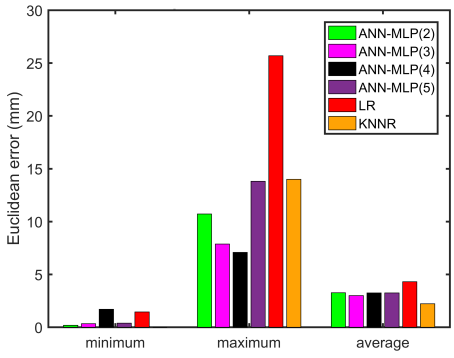


(c) ML models' performance over test data.

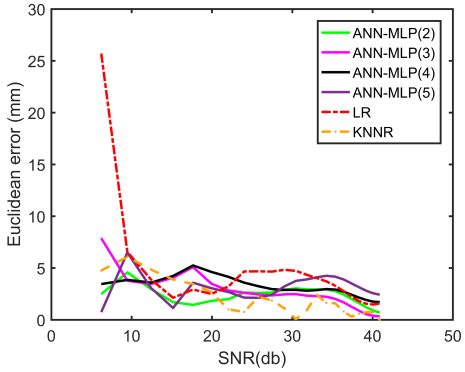


(d) ML models' performance versus radial distance.

Figure 24 – Dynamic range and average accuracy improvements in the beam-tracking task achieved by ML models compared to traditional EQS.



(a) Statistics of models' performance over test data.



(b) Models' error performance versus SNR data.

Figure 25 – Models' analysis based on statistical and prediction error across SNR levels.

from 10 to 40 dB, indicating stable performance under varying noise levels. In contrast, the LR model performance degrades in low-SNR scenarios. The average response time and accuracy for each model are shown in Fig. 26, highlighting the trade-off between speed

and performance. The response times are normalized with respect to the average of the traditional EQS.

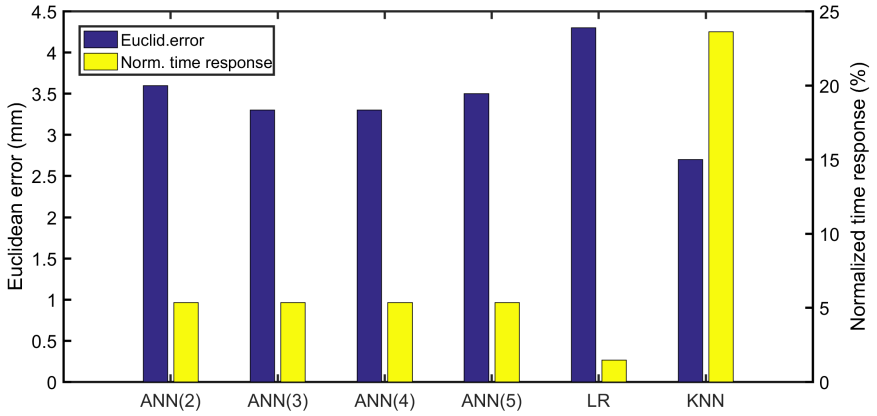


Figure 26 – Model performance comparison: Euclidean error *versus* response time.

Remarkably, the response time of the LR model was 16 times faster than that of the KNN. Notably, the ANN was the only model for which the time response analysis included the processing time required for data normalization and denormalization during prediction. In contrast, for both the LR and KNN models, only the output time response was considered in the training process. In fact, the ANN offers a balanced trade-off between accuracy and response time. Although the response time across ANN topologies did not differ substantially, the 3-2-2 topology requires less memory for storing weight parameters and, consequently, involves fewer operations per neuron unit.

3.3- Conclusion

This study experimentally investigated the application of ML models to enhance the triangulation technique for beam tracking and PE compensation, achieving improved accuracy, dynamic range, reduced response-time overhead, and greater adaptability to noise-biased data through a novel methodological contribution. To highlight the results, the EQS benchmark of approximately 340 ms is used for time response comparison.

KNN achieved the highest accuracy but had a slower response time. This overhead can be reduced by the LR model, which achieved a response time of 5 ms (98.5% faster than EQS). However, because of its deterministic fitting approach, LR performance

degrades in high-SNR scenarios. Offering a balanced trade-off, the ANN models had a 22 % higher error than KNN, however, achieved a time response about 81.5 % faster than traditional EQS, while remaining robust to noisy data.

Note that the experiments were conducted under controlled laboratory conditions, where the PE was emulated via RX-plane movement, rather than through a fully developed AT channel. Therefore, the results represent a proof-of-concept, and future work should assess the models under realistic turbulence scenarios to validate their applicability in field deployments. Finally, this work suggests that the selection of an ML model for FSO beam tracking should be guided by the specific requirements of the system, as each algorithm presents distinct trade-offs between accuracy and time responsiveness. The system accuracy can be further improved by employing an ensemble of ML models implemented on a parallelized FPGA architecture, while models pre-trained with synthetic data can reduce field deployment time.

In summary, the ML-driven optical power triangulation technique was experimentally validated, demonstrating reliable performance in terms of tracking accuracy, response time, and improved dynamic range. As a beam displacement sensing method, the triangulation approach operates under the assumption that a preceding AT-wavefront compensation stage is present within the FSO system. In this context, *Experiment 2*, which will be presented in the next section, addresses this requirement by demonstrating the use of a SLM for effective AT-induced wavefront compensation.

4- Experiments 2 and 3: ML–Driven SLM for wavefront turbulence and pointing error compensation

4.1- ML–Driven SLM for wavefront turbulence

4.1.1 Introduction

To address AT-induced wavefront distortions, SLMs have been experimentally tested in combination with autonomous control algorithms. For instance, P. Chen et al. [37] employed an SLM with an iterative SGD method for AT wavefront compensation. Similarly, H. Chang et al. [38] utilized an SLM together with the GS algorithm to compensate AT-disrupted OAM beams. However, these techniques require derivative computations and fast FFTs, and are inherently iterative, resulting in significant computational overhead. This limits their applicability to real-time FSO systems when compared with ML models approach such as the CNN. Following this approach, W. Xiong et al. [39] used SLMs to emulate AT effects by loading phase masks, while a secondary device applied compensation masks predicted by a CNN to mitigate the induced turbulence in VB and LG beams.

In fact, the SLM is a widely used optical element in FSO systems, serving multiple functions such as generating beam modes for OAM multiplexing, deflecting beams via diffraction gratings, optical switching and beam steering [40]. Their ability to encode custom phase distributions enables manipulation of optical beams, making them suitable for both compensation and multiplexing tasks.

This study proposes an AI-driven CNN model for compensating AT-wavefront distortions by dynamically generating phase masks applied via a SLM. The results show significant improvements in optical power coupling into a standard SMF and effective restoration of the transmitted GB. The work employs the GB mode, known to be less resilient than VB and LG beams [41]. The main contribution of this work is the analysis of irradiance patterns before and after compensation. The results show that the Generalized Extreme Value (GEV) distribution provided provided a better fit than traditional models,

leading to a new insight for FSO system characterization and channel fading modeling.

4.1.2 Theory Background and methodology

Optical beam propagating phase fluctuations

When an optical beam propagates through an AT-channel, it interacts with random refractive-index inhomogeneities, leading to wavefront phase distortions and, consequently, spatial variations in the beam intensity distribution. These distortions originate from air eddies of different sizes and temperatures, which induce stochastic fluctuations in the refractive index along the propagation path.

For the generation of the training dataset, the simulations consider only the phase distortions introduced by AT, which are modeled using turbulence phase screens. Under this assumption, the turbulent spatial distribution of the GB after propagation through the AT channel can be expressed as follows Eq.[29],

$$U_2(x,y) = U_1(x,y).e^{-j\theta(x,y)}, \tag{29}$$

where $U_1(x,y)$ is the initial spatial amplitude of the GB, $\theta(x,y)$ denotes the spatial phase variations induced by the medium, i.e., AT phase mask, and $U_2(x,y)$ is the turbulent beam immediately after AT propagation [49].

The phase mask is generated by resorting to the Monte Carlo Fourier transform method [49], assuming the modified Von Kárman PSD, which is given by Eq.[30],

$$\Phi_n(\theta) = \frac{0.033}{0.423\,L\,k^2}\, r_0^{-5/3} \frac{\exp\left(-\frac{k^2}{k_m^2}\right)}{\left(k^2+k_0^2\right)^{11/6}}, \tag{30}$$

where $k_m = 5.92/l_0$ is the inner scale frequency, $k_0 = 2\pi/L_0$ is the outer scale frequency, L is the transmission link length, and the turbulence strength is controlled by r_0, as shown in Eq.[31],

$$r_0 = (0.423k^2C_n^2L)^{-3/5}, \tag{31}$$

where C_n^2 is the refractive index structure parameter, $k = 2\pi/\lambda$ is the optical wave number,

λ is the wavelength of the light source.

Dataset Generation

The training process of the CNN used pairs of ideal GB transmitted and turbulence-distorted GB, with the corresponding AT phase masks simulated via the modified Von Kármán power spectral density (PSD) as target. Following the described theoretical framework, simulations for AT-phase masks generation were carried out using the values shown in Table 7.

Table 7 – Parameters used for AT phase masks generation for Experiment 2.

Parameters	
Outer scale (L_0)	100 m
Inner scale (l_0)	0.001 m
Coefficient structure index (C_n^2)	$10^{-12}\, m^{-2/3}$
Path length (L)	1 m
Wavelength (λ)	1550 nm

Then, a dataset comprising 1200 AT phase masks was created using MATLAB® software. These masks were loaded onto the SLM screen to impose wavefront distortions on the GB, whose images were captured using a CCD camera at the receiver end of our FSO experimental setup. The dataset was divided into 1000 samples for training the CNN model, 100 for validation, and 100 for testing.

Generative convolutional neural networks

As shown in Fig. 27, the generative CNN for AT-wavefront distortion compensation is an experimental data-driven model. The dataset consists of paired samples: the ideal GB transmitted, representing the received beam without AT but accounting for Fresnel and geometric diffraction (TX); the received beam affected by the AT phase mask (RX); and the AT phase mask itself (Turb mask).

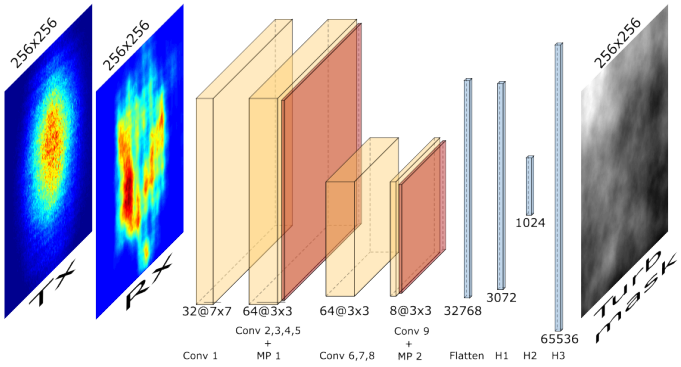


Figure 27 – CNN for AT compensation. Convolutional layers are represented by the yellow block with dimensions, $D@N \times N$, where D represents the depth and $N \times N$ the layer grid dimension; max-pooling layers are indicated by red blocks; fully connected layers are indicated by blue blocks.

The Fig. 28 shows the MSE training loss curve rapidly decreasing within the first few dozen epochs. The models performance can be initially assessed using the validation loss curve, which is computed on data not seen during training. After 200 epochs, the lowest validation loss of 0.0214 was observed at epoch 198. At this point, the neuron weights were frozen and the model was evaluated on a separate test set consisting of 100 samples.

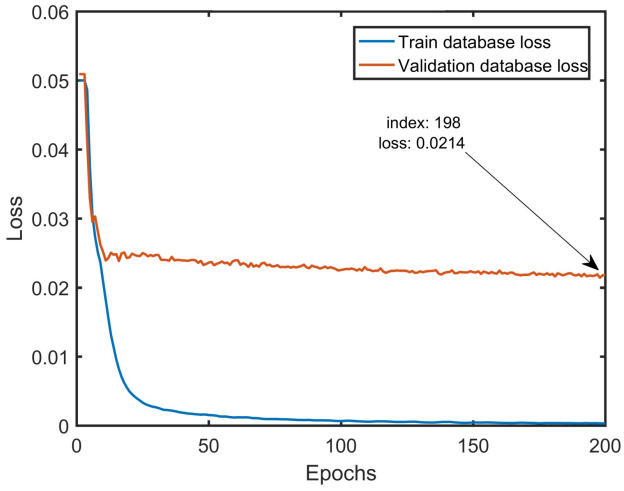


Figure 28 – Evolution of the loss function during CNN training versus epochs.

SLM device and calibration procedures

In this study, all experimental results were obtained using a liquid-crystal-on-silicon spatial light modulator(LCoS-SLM), model PLUTO-2, manufactured by Holoeye.

The Fig. 29 depicts the Holoeye PLUTO-2 LCoS-SLM used in this study. Because the phase–gray-scale response depends on the wavelength and the selected look-up table (LUT), the SLM must be calibrated for each wavelength–LUT pair. The SLM consists of a two-dimensional array of pixelated electrodes that electronically control the orientation of liquid crystal molecules through voltage modulation. Each pixel operates independently and enables spatially resolved phase control via an eight-bit gray-scale input, thereby allowing dynamic wavefront shaping across the SLM aperture.



Figure 29 – Commercial SLM Pluto-2 manufactured by Holoeye.

The response of the SLM phase versus gray scale curve is dependent on the incident wavelength and the programmed look-up table (LUT) in the SLM control software. Therefore, the SLM must be calibrated for each wavelength and LUT combination. Thus, the calibration experiment was conducted using the manufacturers default LUT (sequence 18:6) and using two polarizes oriented at ± 45 degrees to perform a 0 up to 255 gray scale sweep as described in [42–44]. The calibration setup to characterize the SLM with a common path interferometer is shown in Fig.30.

The calibration setup, based on a common-path interferometric configuration, yielded a curve mapping phase modulation as a function of gray-scale level, as shown in Fig. 31. As shown, the phase response does not provide a full 2π modulation for the 1554 nm wavelength used in the experiments.

By experimentally determining the relationship between the induced phase shift and the corresponding gray-scale value, appropriate digital control values can be assigned to accurately generate the desired phase profiles on the SLM, whether for atmospheric turbulence emulation or for PEC. To avoid phase ambiguity and non-injective gray-to-phase mapping, only the monotonic region of the calibration curve was employed. Specifically,

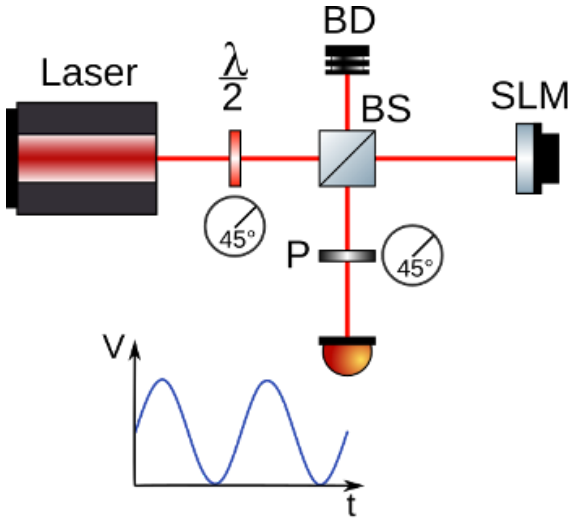


Figure 30 – Phase modulation (π rad) *versus* gray-scale level for the 18:6 LUT at 1554 nm.

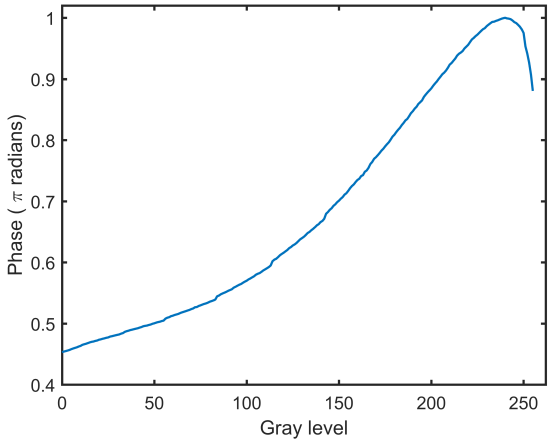


Figure 31 – Resulting phase π radians vs. gray level plot for 18:6 sequence and 1554 nm.

gray-scale values in the range 0–90 were selected, which effectively allow phase modulation up to π radians and ensure stable and unambiguous wavefront control throughout the experiments.

AT-wavefront compensation experiment

The AT-wavefront compensation methodology was evaluated using the experimental setup depicted in Fig. 32. The setup comprises a transmitter emitting a horizontally polarized 1554 nm laser, pigtailed to a polarization-maintaining fiber and coupled to a Thorlabs collimator (F810APC). Then, after passing through the optical components, the beam diameter is approximately 4.1 mm at the $1/e^2$ of its initial level, and is aligned with the

right side of the SLM (Holoeye Pluto 2), which loads the AT phase masks. A 50:50 beam splitter directs the distorted wavefront toward the SMF-coupling path and simultaneously to a CCD beam profile camera (Duma Optronics) that provides feedback for the CNN. This feedback enables adaptive compensation by loading corrective phase masks on the left side of the SLM. The efficiency of the compensation method is assessed by measuring the optical power coupled into the SMF and by modeling the irradiance probability density function (PDF) for both cases: (i) AT-distorted wavefronts and (ii) AT-distorted wavefronts with compensation system enabled.

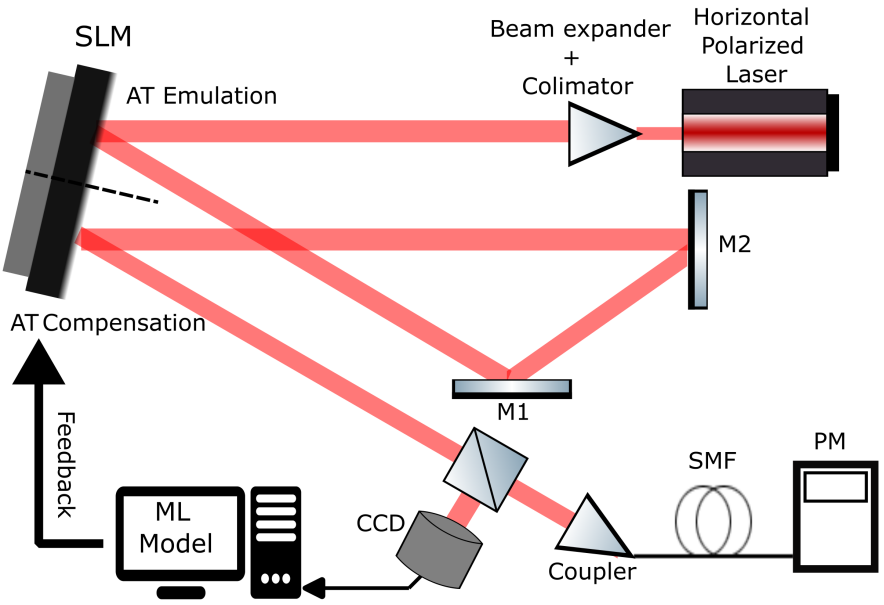


Figure 32 – Experiment diagram: M1 and M2: flat mirrors; SLM: spatial light modulator; CCD: charge-coupled device; SMF: single mode fiber; PM: power meter.

4.1.3 Results

The Fig. 33 presents the coupled optical power into the SMF under three conditions: without AT (black dashed line, labeled as *init.Pot*), with the AT phase mask applied (*Turb.Pot*), and both the AT phase and compensation masks applied (*Comp.Pot*). The degradation of coupled power due to AT is evident. The blue curve illustrates temporal fluctuations in the coupled power corresponding to each loaded AT mask. Subsequently, the CNN predicts these AT masks, and the inverse phase mask is applied to compensate the channel, as shown by the red curve, demonstrating improved coupling efficiency.

Furthermore, the compensation system tends to retrieve most of the original GB waveform, as demonstrated in example of Fig. 34.

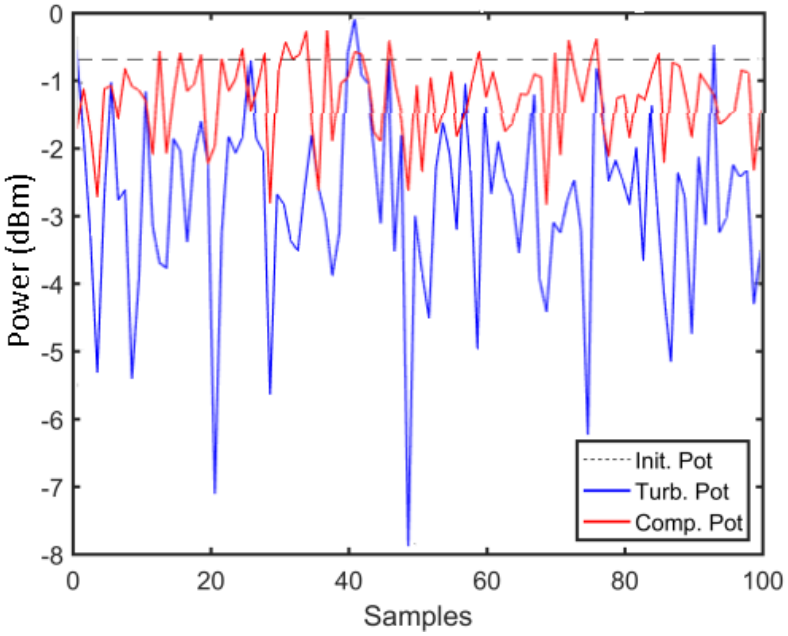
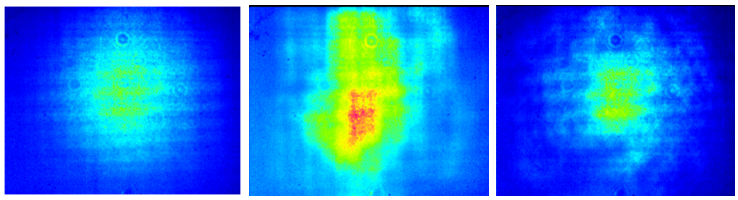


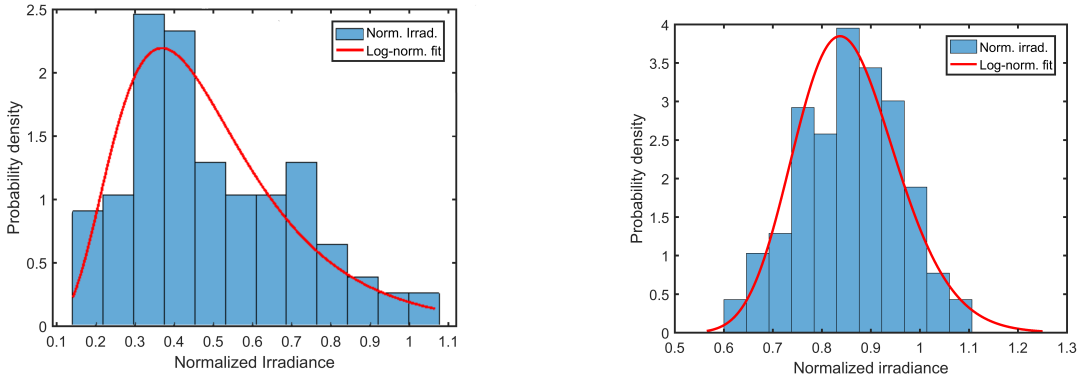
Figure 33 – Coupled power into SMF under different scenarios.



(a) (a) (b) (b) (c) (c)

Figure 34 – Gaussian beam wavefront interacting with the SLM: (a) propagation without atmospheric turbulence, (b) propagation under atmospheric turbulence, and (c) turbulence compensation using the proposed correction method.

Indeed, it is well established that PDFs such as log-normal, Rician, and Gamma distributions are traditionally employed to model the normalized irradiance (NI) fluctuations in FSO links [14]. In Fig. 35(a) under AT-emulated scenario, a sparse distribution is observed, with the mean power ranging from 35% to 40% of the normalized null-AT channel. Conversely, Fig. 35(b) illustrates the compensated AT scenario, where a bell-shaped distribution indicates a mean power delivery of 85–90% relative to the null-AT channel. In this case, the irradiance data are more accurately modeled by the GEV distribution, with $R^2 \approx 0.94$, indicating a strong agreement between the model and the observed data.



(a) (b)

Figure 35 – PDFs of the normalized irradiance: (a) fitted distribution and (b) compensated irradiance.

4.1.4 Conclusion

This work employed a generative CNN to compensate for wavefront distortions in an emulated AT channel. By learning from distorted GB profiles, the CNN generalized the AT phase masks, enhancing SMF coupling efficiency. Additional improvements can be achieved through EDFA pre-amplification and ensemble ML techniques. Regarding the fitting models, the NI data are better modeled by the GEV distribution than by traditional PDFs, indicating a novel model for FSO channel characterization. However, further investigation is needed to relate the GEV parametrization to the Rytov parameter, while the SLM refresh rate and geometric losses remain limitations of the method..

In summary, experiment 2 demonstrates that SLM-based wavefront compensation is an effective strategy for mitigating AT-induced distortions at the receiver, restoring a quasi-Gaussian beam profile and stabilizing the spatial distribution of the received optical field for the tracking stage proposed in experiment 1. Building upon this foundation, experiment 3 leverages the same SLM platform to perform fine PEC, enabling a non-mechanical beam steering through a generative CNN phase mask modulation.

In this combined architecture, wavefront correction reduces the load on traditional electro-mechanical pointing beam mechanisms, while fine optical steering corrects the residual misalignments caused by stressed components. As a result, the integration of experiments 2 and 3 forms a complementary optical control framework that reduces the operational effort of electro-mechanical ATP components, improves system stability, and increases the overall resilience of FSO communication links under varying propagation

conditions.

4.2- ML–Driven SLM for pointing error compensation

4.2.1 Introduction

In the previous sections, the main challenges imposed by the AT-channel were discussed. Impairments such as beam wander, beam spreading, scintillation, and mechanically induced PE, represent limitations to the reliability of FSO links. These effects are primarily mitigated through the use of electro-mechanical systems designed to maintain LOS alignment between FSO transceivers.

Within this context, this thesis presented experiments 1 and 2, which address complementary tasks related to beam tracking and wavefront compensation. In this section, experiment 3 demonstrates an additional application of the SLM, where under the same calibration conditions (LUT sequence 18:6), the SLM is employed for PEC, thereby compensating residual tracking and PE.

Accordingly, a substantial body of literature has addressed strategies for PE mitigation and LOS maintenance. Current ATP methods rely on beam manipulation and pointing solutions typically based on mechatronic components, including gimbals, MEMS, and FSMs [45]. Although effective, these components are subject to mechanical stress and long-term reliability constraints. To enhance system robustness and fault tolerance, redundancy at the physical layer is often required. In this context, SLMs have emerged as a promising complementary technology, enabling hybrid architectures that combine mechanical actuation with adaptive optical control for fine-tuning PEC.

Several studies have explored SLM-based PEC strategies. For example, Niu et al. [33] employed a CCD camera at the receiver to estimate beam centroid displacement and generated blazed gratings on an SLM to compensate PE via diffraction. Similarly, Spaander et al. [34] combined phase ramp gratings with Fresnel lenses loaded onto an SLM to counteract mechanically induced PE, while Goto et al. [35] demonstrated SLM-based beam steering for coupling into multi-core fibers. However, grating-based approach inherently introduce unwanted diffraction orders due to pixel voltage leakage

and power scattering, resulting in deviations from the ideal optical response and reduced power efficiency.

Beyond these issues related to grating-based approach, the AT-channel update rate further constrains SLM-based solutions. Non-analytical control methods, such as SGD and the GS algorithm, require multiple iterations to converge, leading to significant computational overhead and limiting their applicability in rapidly varying channels [36, 37, 46, 47]. Although effective under quasi-static conditions, such methods become impractical for turbulence dynamics on the order of kilohertz. In contrast, ML models, particularly feedforward CNNs, offer a compelling alternative by enabling fast, non-iterative inference [48].

Motivated by these limitations, this experimental investigation explores the use of an SLM combined with ML-based control to maintain precise alignment between FSO transceivers. The goal is to compensate mechanically induced pointing errors (PE), including residual PE caused by fatigue in mechatronic components used in conventional ATP systems (gimbals, MEMS, and FSMs), which can reduce fine-pointing accuracy.

Specifically, the experiment introduces a novel approach in which a CNN model dynamically generates phase masks applied to an SLM, enabling controlled beam diffraction for PEC and improving optical power coupling into a standard SMF and reducing computational overhead by eliminating the use of iterative optimization methods.

Experimental results demonstrate an optical power improvement of up to 34 dB under a beam misalignment of 0.5 mm at the receiver, corresponding to approximately 0.01° of PE at the transmitter over a 2.5 m link length. Furthermore, the proposed SLM-based PEC approach maintains effective compensation for misalignments up to 4.8 mm ($\approx 0.11^\circ$), confirming its practical viability for dynamic fine-tuning PE mitigation in FSO communication systems.

4.2.2 Theory background and methodology

Dataset generation

Similarly to experiment 2, during training, the CNN learns the mapping between turbulence-induced phase distortions and their resulting impact on the propagated beam

output. Once trained, the model is capable of generating appropriate phase masks that manipulate the optical wavefront, enabling controlled beam deflection and effective PEC. Thus, a set of 1200 pairs of input and output samples, of which 1000 samples used for training, 100 for validation, and 100 for testing, was generated assuming the modified Von Kárman PSD modeled in MATLAB. The phase masks were generated using the parameters listed in Table 8.

Table 8 – Parameters used for AT phase masks generation for experiment 3.

Parameters	
Outer scale (L_0)	100 m
Inner scale (l_0)	0.001 m
Coefficient structure index (C_n^2)	$10^{-13}\, m^{-2/3}$
Path length (L)	1 m
Wavelength (λ)	1550 nm

Generative convolutional neural networks

The generative CNN model for PEC was trained using a simulated dataset comprising input pairs: the GB (TX sim), which represents the experimental received beam without turbulence but accounts for Fresnel-diffraction, and the received beam affected by the AT phase mask (RX sim); the AT phase mask (turb mask) used as the output, as shown in Fig. 36. Note that the inputs, i.e., TX sim and RX sim, images represent "what we have" immediately after transmission and "what is received" at the receiver.

The CNN was trained with 1000 samples for 25 epochs. This limit is based on experimental observations of the MSE loss curve from multiple trained models, as shown Fig. 37, which asymptotically stabilizes with small variations of order 10^{-4}, justifying the decision to stop training and avoid overhead. In this CNN model, conventional early stopping based on a validation dataset analysis is not applicable due to the distinct patterns between training and test output data.

After training, the model generalizes beam source manipulation by learning how AT distorts the optical wavefront, owing to the inherent flexibility provided by the CNN-learned model, which can effectively decouple wavefront distortions from PE, enabling the generation of phase masks for radial PEC. During the CNN test stage, the input order is

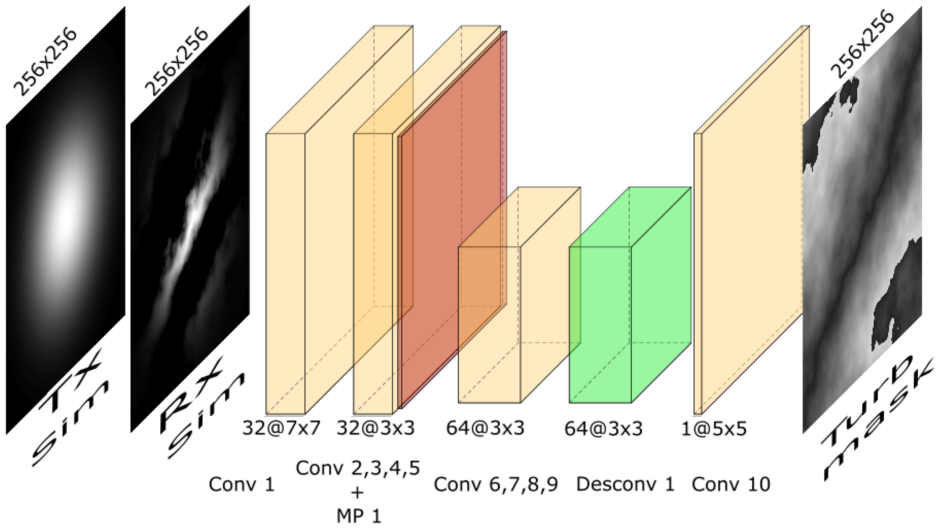


Figure 36 – CNN model for PEC. Convolutional and deconvolutional layers are represented by the yellow and green blocks, respectively, with dimensions, $D@N \times N$, where D represents the depth and $N \times N$ the layer grid dimension; max-polling layers are indicated by red blocks.

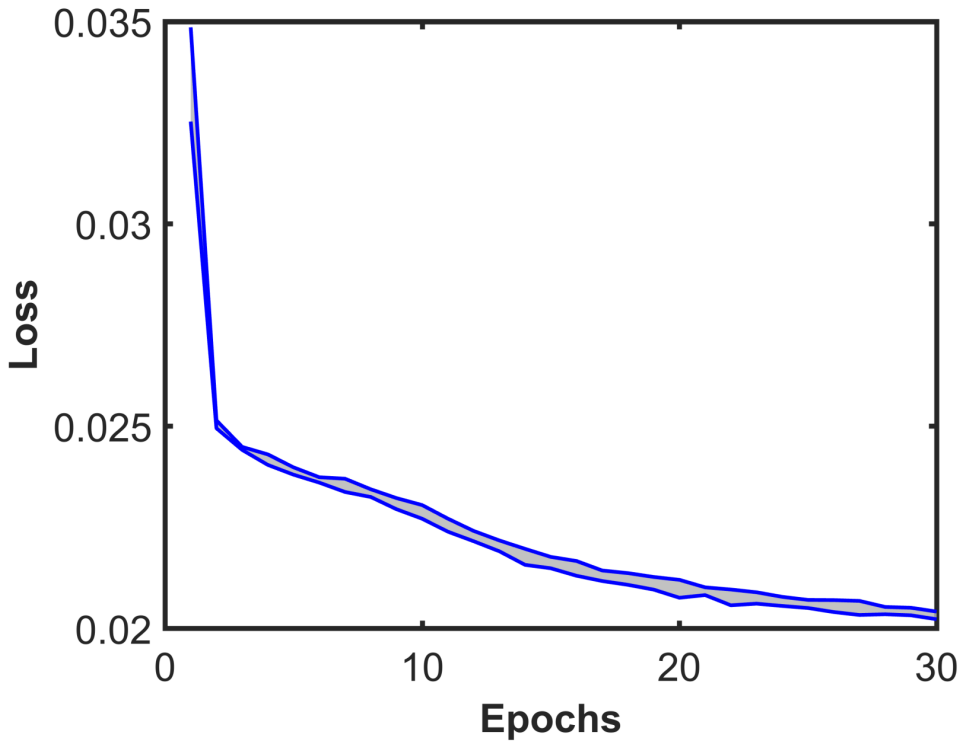


Figure 37 – Evolution of the loss function during the CNN training stage versus the number of epochs.

swapped (RX + TX), providing the model with information about the measured (misaligned) beam / the desired (centered) reference beam (i.e., the received, misaligned beam) and the ideal centralized beam to generate the appropriate PEC phase mask. The Fig. 38

illustrates the operational test stage of the CNN for PEC.

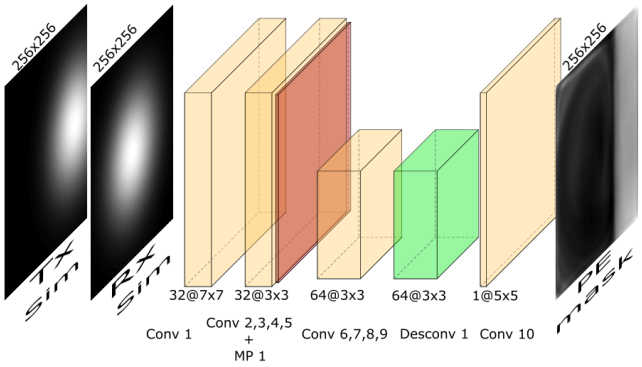


Figure 38 – CNN PE compensation model test stage.

Based on this framework, the proposed PEC system exploits feedback from the receiver, where the beam centroid position is measured using either a CCD camera or a quadrant detector (QD). This information is used to generate a simulated GB with a corresponding spatial displacement, which is paired with an ideal, centered reference beam, as illustrated in Fig. 37. These beam pairs constitute the input to the CNN model for the generation of phase masks dedicated to PEC. The resulting PEC phase masks are subsequently uploaded to the SLM to manipulate the transmitted wavefront.

Accurate phase modulation by the SLM requires a precise correspondence between the applied gray-scale values and the phase shifts induced on the optical wavefront. Consequently, a dedicated calibration procedure is essential prior to system operation to ensure the correct mapping between digital control values and the resulting phase modulation.

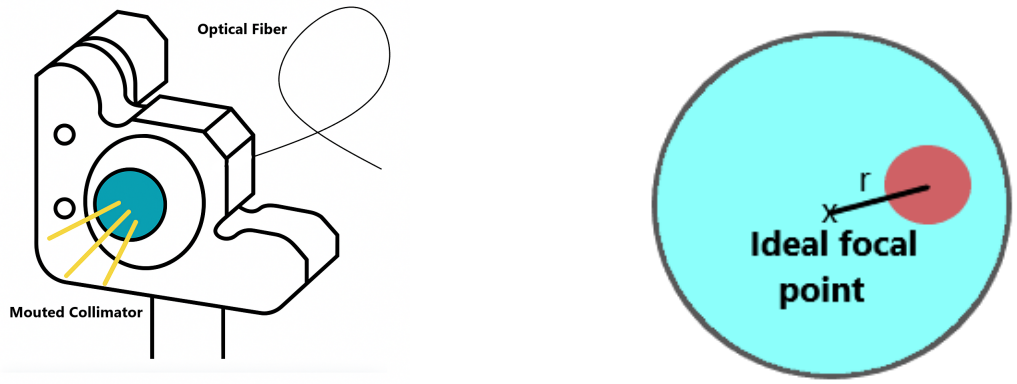
PE definition

Maintaining continuous line-of-sight (LOS) is critical in fiber-coupled FSO receivers, where the collected optical power is directly injected into the fiber core. In SMF systems, the core diameter (approximately 8–10 μm) acts as a stringent spatial filter, rendering the link highly sensitive to PE. For a fixed PE (boresight error), the coupled optical power decays according to Eq. [32],

$$P = e^{-\left(\frac{r}{W}\right)^2}, \tag{32}$$

where r denotes the radial displacement from the receiver collimator axis and W is the Gaussian beam radius at the receiver, defined at the $1/e^2$ power level.

Figure 39a illustrates a typical collimator lens directly coupled to an optical fiber, highlighting the role of the fiber core as a highly selective spatial aperture. As a result, even small beam misalignments lead to significant coupling losses and power fading. This effect is further depicted in Fig. 39b, which shows a tightly focused spot at the receiver plane, where any deviation from the optimal focal position constitutes a PE and directly degrades the optical power coupled into the SMF [7].



(a) Collimators directly coupled to the fiber. (b) Radial displacement origin PE.

Figure 39 – Representative schema of a typical FSO receiver.

In summary, PEs can be quantitatively described by the radial displacement (r) of the beam centroid from the optical axis, as illustrated in Fig. 39b. This displacement arises predominantly from beam wander caused by refractive-index fluctuations in an AT-channel and is further aggravated by mechanical instabilities and imperfections in tracking and alignment subsystems. The objective of the experimental setup presented in the next section is to mitigate PEs independently of their underlying origin by exploiting the SLM and the generative CNN to compute PEC masks.

Experimental setup

The PEC methodology is initially tested by manually rotating a flat mirror using a micrometer screw to generate horizontal displacements, and the CNN computes a PEC phase mask to optimize SMF-coupled power in the FSO setup. The first experimental setup is shown in Fig. 40. It consists of a transmitter with a horizontally polarized 1554

nm laser pigtailed to a polarization-maintaining fiber, connected to a Thorlabs collimator (F810APC). After propagating over 2.5 m and passing through the optical components, the beam measures ø 4.1 mm at $1/e^2$, and aligns with the SLMs horizontal axis. The setup includes a Holoeye Pluto 2 SLM, a movable flat mirror (M1) for horizontal beam displacement, and a power meter (PM) to measure SMF-coupled optical power at the receiver, which uses the same collimator model. A 50:50 splitter directs the beam to a CCD camera (Duma Optronics), which senses displacement and provides input to the CNN model for PEC feedback.

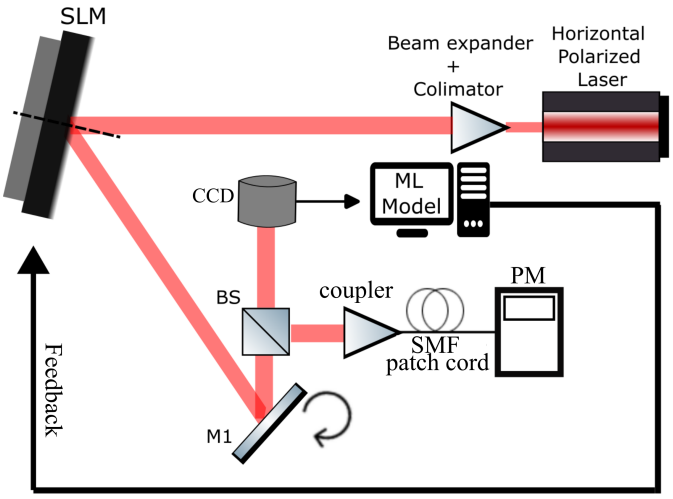


Figure 40 – Schematic diagram of the experimental setup. M1: movable flat mirror; SLM: spatial light modulator; CCD: charge-coupled device; BS: beam splitter; SMF: single-mode fiber; PM: power meter.

Subsequently, the experimental setup was upgraded by integrating a motorized support for M1 using a Thorlabs ZST206 stepper motor actuator and replacing the CCD with a Thorlabs PDQ30C QD, as shown in Fig. 41.

By automating the mirror actuation, the system enables a systematic and repeatable evaluation of the proposed compensation strategy over a wide range of controlled radial displacements induced by the motorized mirror M1. This automated procedure ensures consistent testing conditions and provides a robust basis for performance assessment. The corresponding experimental results and their analysis are presented in the following section.

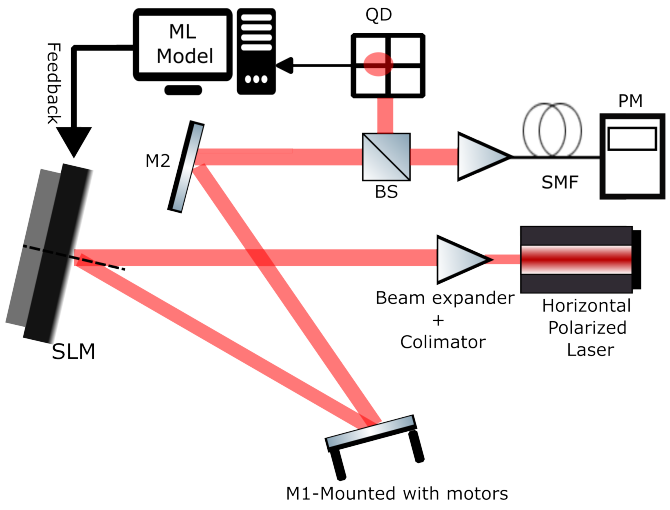


Figure 41 – Schematic diagram of the updated experimental setup. M1: movable flat mirror; M2: fixed flat mirror; SLM: spatial light modulator; BS: beam splitter; QD: quadrant position-sensing detector; SMF: single-mode fiber; PM: power meter.

4.2.3 Results

Using the trained CNN models, controlled horizontal misalignments ranging from 0.1 to 2.5 mm were introduced with the first experimental setup. Each operating condition was evaluated in triplicate by training three independent CNN instances; all results reported below are statistical averages over these realizations. For each misalignment step, the beam centroid position measured at the receiver is fed back to the control unit, which emulates the corresponding displaced Gaussian beam and provides it as input to the CNN. The network then generates the appropriate PEC phase mask, which is uploaded to the SLM to improve optical power coupling into the SMF.

It is worth noting that the application of the predicted PEC masks modifies the original wavefront shape, as illustrated in Fig. 42. While diffraction-based beam redirection efficiently concentrates optical energy onto the fiber core, it also results in beam narrowing. Consequently, this approach may be less suitable for systems that require strict wavefront preservation, such as mode-division multiplexing schemes based on OAM.

In the results shown in Fig. 43, the coupled optical power was measured under PE conditions (blue bars) and after applying the corresponding compensation phase mask on the SLM screen (yellow bars). The optical power attenuation follows a pattern similar to a GB profile, where the beam gradually attenuates along the displacement distance. With the PEC system activated, the beam profile is enlarged, mitigating attenuation caused by



Figure 42 – From left to right: displaced GB (0.5 mm), PEC phase mask, and corresponding resulting effect.

PE. Notably, the PEC system continued to provide gains even for distances exceeding 1 mm, where the -57 dBm threshold of the PM was reached, indicating the FSO link was outside the LOS capture range.

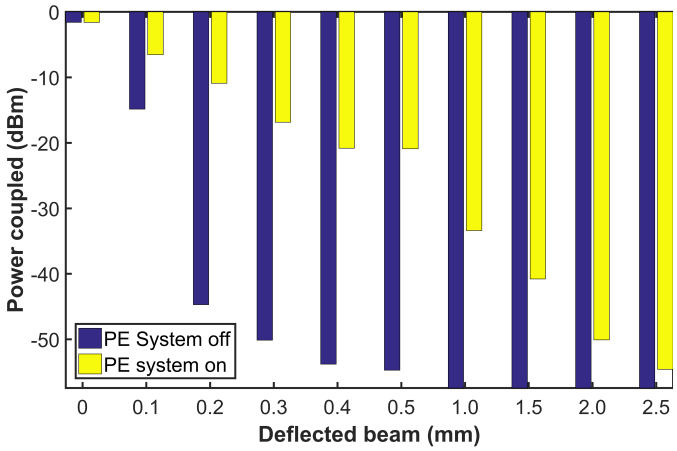


Figure 43 – Optical power coupled in SMF with PEC ON and OFF.

The Fig. 44 presents the system gain for each beam displacement. The PEC system demonstrated effectiveness for displacements up to 2.5 mm, with peak gains of approximately 34 dB observed in the 0.2–0.5 mm range. This highlights the system's capability to restore optical power.

To explore the scalability, diversity, and flexibility of the PEC system, the upgraded experimental setup was employed to autonomously generate 150 distinct random radial displacements up to 4.8 mm without human intervention. The results were analyzed using descriptive statistics, as illustrated in Fig. 45.

The results show an average gain of about 15 dB across all intervals, with a maximum gain of 34 dB in the [0-1] mm range, aligning with the previous results presented in Fig. 44. The presented results can directly improve the performance of FSO system metrics, such as BER, resulting in higher SNR and, hence, larger data throughput.

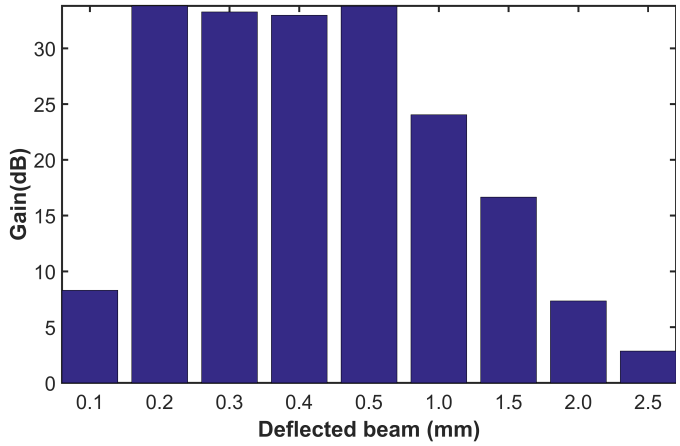


Figure 44 – Gain versus distance displacement.

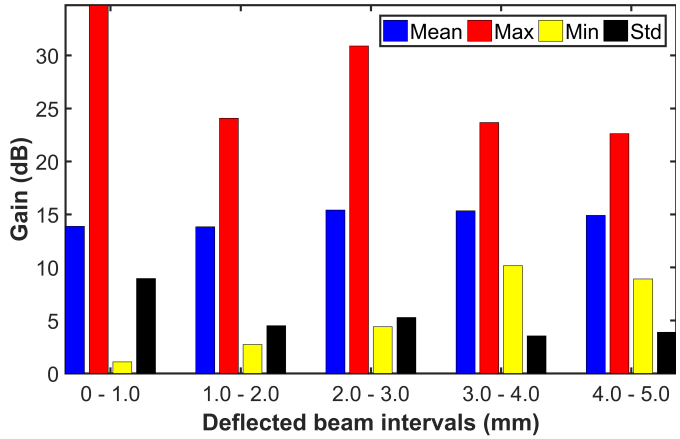


Figure 45 – Descriptive statistical analysis of gain values of the PEC system across a wide range of radial displacement.

4.2.4 Conclusion

This work proposes an AI-driven methodology for PEC by combining a SLM with a generative CNN-based diffraction phase mask. Experimental results demonstrate improvements in fiber coupling efficiency, achieving a maximum gain of 34 dB for a 0.5 mm beam displacement and an average gain of 15 dB compensation up to 4.8 mm in the automated analysis. These results highlight the potential of AI-based strategies to enhance physical-layer reliability in FSO systems by complementing traditional mechatronic PEC methods. Although the CNN introduces computational overhead, particularly for real-time applications, future implementations may benefit from optimized CNN architectures or FPGA-based acceleration. In this study, however, the primary bottleneck was the SLM (Holoeye Pluto 2), limited to 1 Hz refresh rate combined with the constraints of the HDMI

connection supporting a transmission rate of 60 Hz. The demonstrated capability of AI models to generalize optical beam manipulation suggests promising directions for non-analytical wavefront modulation.

T|he proposed approach operates as a receiver-side fine-pointing subsystem, specifically targeting residual misalignments. As such, it is well suited for integration with conventional ATP architectures based on gimbals, fast-steering mirrors, or MEMS devices, where the SLM-based PEC provides optical correction without introducing additional mechanical stress. This hybrid perspective highlights the role of AI-driven wavefront modulation as a complementary and redundant element rather than a replacement for existing mechatronic solutions.

5- Thesis conclusion

This thesis presents three experiments demonstrating the feasibility and effectiveness of ML techniques integrated with optical hardware to improve the performance and reliability of physical-layer FSO communication systems. By addressing the main impairments caused by AT and PE, this work proposes and validates ML-based strategies for the beam ATP method and wavefront correction at the RX-side.

Experiment 1 investigated ML-assisted beam tracking using optical power triangulation for PE compensation. The results demonstrated that data-driven models significantly improve responsiveness range and noise adaptability compared to the traditional EQS method. In particular: LR achieved a response time of 5 ms, corresponding to a 98.5% reduction relative to EQS. The KNN achieved the highest accuracy, at the cost of higher computational latency. And ANNs provided a balanced trade-off, exhibiting strong robustness under noisy conditions with substantially reduced response time compared to EQS. Although the experiments were conducted under controlled laboratory conditions with RX-plane displacement emulating PE (rather than a fully developed turbulence channel), the results establish a clear proof-of-concept for ML-enhanced ATP systems. Field validation under realistic AT conditions remains a necessary next step.

Experiment 2 addressed AT-induced wavefront distortions through the integration of a CNN with a SLM. The proposed compensation strategy restored the spatial integrity of the received beam, increasing the average optical coupling efficiency from approximately 35–40% to 85–90% of the ideal no-turbulence condition. In addition to performance gains, statistical analysis demonstrated that the GEV distribution provides an accurate model for irradiance fluctuations under turbulence. These findings position wavefront correction as a critical optical front-end stage that enhances downstream ATP effectiveness.

Experiment 3 focused on fine PE compensation using an SLM driven by a generative CNN capable of learning the nonlinear mapping between beam displacement and phase-mask synthesis. The proposed approach achieved optical power gains of up to 34 dB for a 0.5 mm misalignment and maintained significant robustness for displacements up to 4.8 mm. This fine optical steering mechanism reduces reliance on purely electro-

mechanical ATP devices and introduces redundancy at the optical layer, thereby increasing overall system robustness.

In summary, the three experimental validated the integration between ML and optical hardware produced consistent and complementary performance improvements. The ML-assisted tracking approach reduced the response time by 98.5% compared to the EQS method. The turbulence compensation strategy increased the optical coupling efficiency from approximately 35–40% to 85–90% of the ideal no-turbulence condition. Additionally, the fine steering method achieved optical power gains of up to 34 dB for small misalignments, maintaining robustness for beam displacements of up to 4.8 mm. Collectively, these results demonstrate that RX-side ML-assisted optical processing significantly improves both dynamic alignment and turbulence mitigation in FSO communication systems.

A practical hardware limitation identified in this work is the refresh-rate constraint of the SLM, approximately 1 Hz in the implemented configuration. Although sufficient for proof-of-concept validation, this restriction limits applicability in fast-varying real-time turbulence scenarios and motivates the adoption of hardware-accelerated processing and higher-speed optical modulation platforms such as based on micromirror arrays .

From a system-level perspective, the thesis establishes that the integration of RX-side ML with adaptive optical elements forms a coherent beam ATP chain. The architecture combines coarse tracking through ML-assisted triangulation, wavefront correction using CNN-based SLM compensation, and fine steering via generative phase-mask synthesis. This layered optical–computational approach reduces dependence on mechanical actuators, increases robustness to stochastic channel dynamics, and enables scalable intelligent FSO receivers.

Future work includes time processing improvement implementation through FPGA acceleration to achieve low-latency inference and higher operational bandwidth, development of fully optical ANN and LR architectures in photonic integrated circuits for faster tracking decisions, investigation of dual-SLM configurations separating wavefront correction and PEC, and extension of the proposed techniques to OAM multiplexing for capacity enhancement in spatially multiplexed FSO links.

Bibliography

[1] "Volume of data or information created, captured, copied, and consumed worldwide from 2010 to 2029 (in zettabytes)." Chart. November 14, 2025. Statista. Accessed December 21, 2025. https://www.statista.com/statistics/871513/worldwide-data-created/

[2] Wang, G.; Yang, F.; Song, J.; Han, Z. Free space optical communication for inter-satellite link: Architecture, potentials and trends. *IEEE Communications Magazine*, vol. 62, no. 3, pp. 110–116, Mar. 2024. doi:10.1109/MCOM.002.2300024.

[3] Chen, R.; Yan, B.; Chang, M.-C. F. A review of circuits and systems for advanced sub-THz transceivers in wireless communication. *Electronics*, vol. 14, no. 5, p. 861, 2025. doi:10.3390/electronics14050861.

[4] Al-Samman, A. M.; Azmi, M. H.; Al-Gumaei, Y. A.; Al-Hadhrami, T.; Abd. Rahman, T.; Fazea, Y.; Al-Mqdashi, A. Millimeter wave propagation measurements and characteristics for 5G system. *Applied Sciences*, vol. 10, no. 1, p. 335, 2020. doi:10.3390/app10010335.

[5] Quan, Y.; Shahsavari, S.; Rosenberg, C. Planning and operation of millimeter-wave downlink systems with hybrid beamforming. *IEEE Transactions on Wireless Communications*, vol. 23, no. 12, pp. 18214–18227, Dec. 2024. doi:10.1109/TWC.2024.XXXXX.

[6] Fortune Business Insights, Free Space Optical (FSO) Communication Market Size, Share & Industry Analysis, By Type (Terrestrial FSO, Airborne and Space FSO, and Underwater FSO), By Range (Short, Medium, and Long), By Component (Transmitter Assembly and Receiver Assembly), By Application (Mobile Backhaul, Enterprise Connectivity, Satellite, Defense, Disaster Recovery, and Others), and Regional Forecast, 2024–2032, report no. FBI107891, last updated December 1, 2025, accessed March 19, 2026, https://www.fortunebusinessinsights.com/free-space-optics-fso-communication-market-107891

[7] Guiomar, F. P.; Fernandes, M. A.; Nascimento, J. L.; Rodrigues, V.; Monteiro, P. P. Coherent free-space optical communications: Opportunities and chal-

lenges. *Journal of Lightwave Technology*, vol. 40, no. 10, pp. 3173–3186, 2022. doi:10.1109/JLT.2022.3164736.

[8] Bittar, F. B.; Garrido, M.; Barbero, A. P. L.; Ferreira, T. N.; Silva, V. N. H. Machine learning algorithms for triangulation-based optical beam tracking in FSO systems. *Optics and Lasers in Engineering*, vol. 196, Art. no. 109397, 2026.

[9] Bittar, F. B.; Fernandes, G. M.; Barbero, A. L.; Monteiro, P. P.; Guiomar, F. P.; Silva, V. N. H. AI-driven atmospheric turbulence compensation and channel modeling in FSO systems. *Proceedings of the 2025 SBFoton International Optics and Photonics Conference (SBFoton IOPC)*, São Pedro, Brazil, pp. 1-3, 2025.

[10] BITTAR, F. B., CORREIA, V. F., FERNANDES, G. M., BARBERO, ANDRÉS L., MONTEIRO, P. P., GUIOMAR, F. P., HENRIQUE SILVA, V. N. Mitigation of Pointing Errors in FSO Systems Through AI-Driven Spatial Light Modulation. *IEEE Photonics Technology Letters*, vol. 37, Art. no. 16, pp. 925-928, 2025.

[11] Roberto Ramirez-Iniguez, Sevia M. Idrus and Ziran Sun, "Optical Wireless Communications IR for Wireless Connectivity", Taylor & Francis Group, Book, CRC Press, 2007.

[12] Trichili, A.; Cox, M. A.; Ooi, B. S.; Alouini, M.-S. Roadmap to free space optics. *Journal of the Optical Society of America B*, vol. 37, pp. A184–A201, 2020.

[13] Andrews, L.; Phillips, R. *Laser Beam Propagation Through Random Media*. SPIE Press, 2005. doi:10.1117/3.626196.

[14] Ghassemlooy, Z.; Popoola, W.; Rajbhandari, S. *Optical Wireless Communications: System and Channel Modelling with MATLAB*. CRC Press, 2019.

[15] Muhamedyev, R. Machine learning methods: An overview. *CMNT*, vol. 19, pp. 14–29, 2015.

[16] McCulloch, W. S.; Pitts, W. A logical calculus of the ideas immanent in nervous activity. *Bulletin of Mathematical Biology*, vol. 52, pp. 99–115, 1990.

[17] Hornik, K.; Stinchcombe, M.; White, H. Universal approximation of an unknown mapping and its derivatives using multilayer feedforward networks. *Neural Networks*, vol. 3, no. 5, pp. 551–560, 1990.

[18] Haykin, S. *Redes Neurais: Princípios e Prática*. Artmed, 2007.

[19] Pedregosa, F.; Varoquaux, G.; Gramfort, A.; et al. Scikit-learn: Machine learning in Python. *Journal of Machine Learning Research*, vol. 12, pp. 2825–2830, 2011.

[20] Majumdar, A. K. *Advanced Free Space Optics (FSO): A Systems Approach*. Springer, 2014.

[21] Muta, S.; Tsujimura, T.; Izumi, K. Laser beam tracking system for active free-space optical communication. In: *Proc. IEEE/SICE International Symposium on System Integration*, pp. 879–884, 2013. doi:10.1109/SII.2013.6776628.

[22] Malak, S.; Hajjar, H. A.; Dupont, E.; Khan, M. U.; Prelle, C.; Lamarque, F. Optical localization and tracking method of a mobile micro-conveyor over a smart surface. *IEEE Sensors Journal*, vol. 21, no. 9, pp. 10618–10627, 2021. doi:10.1109/JSEN.2021.3062731.

[23] Liu, W.; Chen, S.; Huang, N.; Gong, C.; Chen, Y.; Xu, Z. A real-time MEMS mirror-based beam steering and tracking system for optical wireless communication. *Journal of Lightwave Technology*, vol. 43, no. 6, pp. 2681–2689, 2025.

[24] Matsumoto, M.; Osawa, K.; Hotta, S.; Wakamori, K. Innovative tracking system for next generation FSO systems under massive earthquakes. In: *Proc. International Conference on Optical Network Design and Modeling (ONDM)*, pp. 233–238, 2015. doi:10.1109/ONDM.2015.7127304.

[25] Raj, A. Mono-pulse tracking system for active free-space optical communication. *Optik – International Journal for Light and Electron Optics*, vol. 127, 2016. doi:10.1016/j.ijleo.2016.05.143.

[26] Chi, N.; Jia, J.; Hu, F.; Zhao, Y.; Zou, P. Challenges and prospects of machine learning in visible light communication. *Journal of Communications and Information Networks*, vol. 5, no. 3, pp. 302–309, 2020. doi:10.23919/JCIN.2020.9200893.

[27] Liu, J.; Wang, P.; Zhang, X.; He, Y.; Zhou, X.; Ye, H.; Li, Y.; Xu, S.; Chen, S.; Fan, D. Deep learning based atmospheric turbulence compensation for orbital angular momentum beam distortion and communication. *Optics Express*, vol. 27, no. 12, pp. 16671–16688, 2019. doi:10.1364/OE.27.016671.

[28] Wang, H.; Zhan, Z.; Hu, F.; et al. Intelligent optoelectronic processor for orbital angular momentum spectrum measurement. *PhotoniX*, vol. 4, no. 9, 2023. doi:10.1186/s43074-022-00079-9.

[29] Fu, T.; Zhang, J.; Sun, R.; et al. Optical neural networks: Progress and challenges. *Light: Science & Applications*, vol. 13, Art. no. 263, 2024. doi:10.1038/s41377-024-01590-3.

[30] Ding, J.; Liu, T.; Xu, T.; Hu, W.; Popov, S.; Leeson, M. S.; Zhao, J.; Xu, T. Intra-channel nonlinearity mitigation in optical fiber transmission systems using perturbation-based neural network. *Journal of Lightwave Technology*, vol. 40, no. 21, pp. 7106–7116, 2022. doi:10.1109/JLT.2022.3200827.

[31] Campos, A. C.; Georgieva, P.; Fernandes, M. A.; Monteiro, P. P.; Fernandes, G. M.; Guiomar, F. P. Optical beam steering in FSO systems supported by computer vision. *IEEE Access*, vol. 12, pp. 73793–73809, 2024. doi:10.1109/ACCESS.2024.3405196.

[32] Silva, V.; Barbero, A.; Ribeiro, R. A new triangulation-like technique for the evaluation of the refractive index structure constant (C_n^2) in free-space optical links. *Journal of Lightwave Technology*, vol. 29, pp. 3603–3610, 2011. doi:10.1109/JLT.2011.2167128.

[33] Niu, Q.; Wang, C. High precision beam steering using a liquid crystal spatial light modulator. *Optical and Quantum Electronics*, vol. 51, 2019.

[34] Spaander, J.; Guo, J.; Saathof, R.; Gill, E. Reducing beam tracking complexity using a phase ramp and Fresnel lens when steering beams using spatial light modulators. *Optics Letters*, vol. 49, 2024.

[35] Goto, Y.; Shinada, S.; Hirota, Y.; Furukawa, H. LCOS-based flexible optical switch for heterogeneous SDM fiber networks. In: *Proc. 24th Int. Conf. on Transparent Optical Networks (ICTON)*, 2024.

[36] Chang, H.; Yin, X.; Cui, X.; et al. Adaptive optics compensation of orbital angular momentum beams with a modified Gerchberg–Saxton-based phase retrieval algorithm. *Optical Communications*, vol. 405, 2017.

[37] Chen, P.; Yu, W.; Guo, Y.; et al. A novel Sophia-SPGD optimization method for wavefront correction in WFS-less AO systems. *Photonics*, 2025.

[38] Chang, H.; Yin, X.; Cui, X.; Zhang, Z.; Ma, J.; Wu, G.; Zhang, L.; Xin, X. Adaptive optics compensation of orbital angular momentum beams with a modified Gerchberg–Saxton-based phase retrieval algorithm. *Optical Communications*, vol. 405, 2017.

[39] Xiong, W.; Wang, P.; Cheng, M.; Liu, J.; He, Y.; Zhou, X.; Xiao, J.; Li, Y.; Chen, S.; Fan, D. Convolutional neural network based atmospheric turbulence compensation for optical orbital angular momentum multiplexing. *Journal of Lightwave Technology*, 2020.

[40] Hu, C.; Chen, C.; Lee, Y.; Wu, H.; Lin, S.; Tsau, H.; Horng, J. Prototype and analysis of solid-state beam steering using spatial light modulator for LiDAR. In: *Proc. SPIE Future Sensing Technologies*, 2024.

[41] Yuan, Y.; Lei, T.; Li, Z.; Li, Y.; Gao, S.; Xie, Z.; Yuan, X. Beam wander relieved orbital angular momentum communication in turbulent atmosphere using Bessel beams. *Scientific Reports*, 2017.

[42] Browar, A. E. M.; Shusteff, M.; Kelly, B. E.; et al. Overview and comparison of spatial light modulator calibration methods. *Proceedings of the ASPE Annual Meeting*, pp. 293–299, 2016.

[43] Balondrade. Paul and Popoff. Sébastien M., "Calibration of Linearly Aligned Nematic Liquid Crystal based Spatial Light Modulators". Sep. 21, 2018. [Online]. Available: https://www.wavefrontshaping.net/post/id/22

[44] Farré, A.; Shayegan, M.; López-Quesada, C.; et al. Positional stability of holographic optical traps. *Optics Express*, vol. 19, pp. 21370–21384, 2011.

[45] Milaševičius, M.; Mačiulis, L. A review of mechanical fine-pointing actuators for free-space optical communication. *Aerospace*, vol. 11, no. 1, Art. no. 5, 2024. doi:10.3390/aerospace11010005.

[46] Wu, J.; Ke, X.; Yang, Y.; Liang, J.; Liu, M. Correction of distorted wavefront using dual liquid crystal spatial light modulators. *Photonics*, 2022.

[47] Hu, C.; Chen, C.; Lee, Y.; et al. Prototype and analysis of solid-state beam steering using spatial light modulator for LiDAR. In: *Proc. SPIE Future Sensing Technologies*, 2024.

[48] Madsen, A.; Eriksen, R.; Glückstad, J. Comparison of state-of-the-art computer-generated holography algorithms and a machine learning approach. *Optical Communications*, vol. 505, 2022.

[49] Schmidt, J. D. *Numerical Simulation of Optical Wave Propagation with Examples in MATLAB*. SPIE Press, 2010.

[50] Alimi, I.; Shahpari, A.; Sousa, A.; et al. *Challenges and Opportunities of Optical Wireless Communication Technologies*. IntechOpen, 2017.

[51] Bekkali, A.; Fujita, H.; Hattori, M. New generation free-space optical communication systems with advanced optical beam stabilizer. *Journal of Lightwave Technology*, vol. 40, no. 5, pp. 1509–1518, 2022.